

SPRig: Self-Supervised Pose-Invariant Rigging from Mesh Sequences

Ruipeng Wang*
 University of Pennsylvania
 Philadelphia, USA
 ruipeng@sas.upenn.edu

Langkun Zhong*
 The University of Hong Kong
 Hong Kong, China
 zhong.langkun@outlook.com

Miaowei Wang
 The University of Edinburgh
 Edinburgh, UK
 s2608314@ed.ac.uk

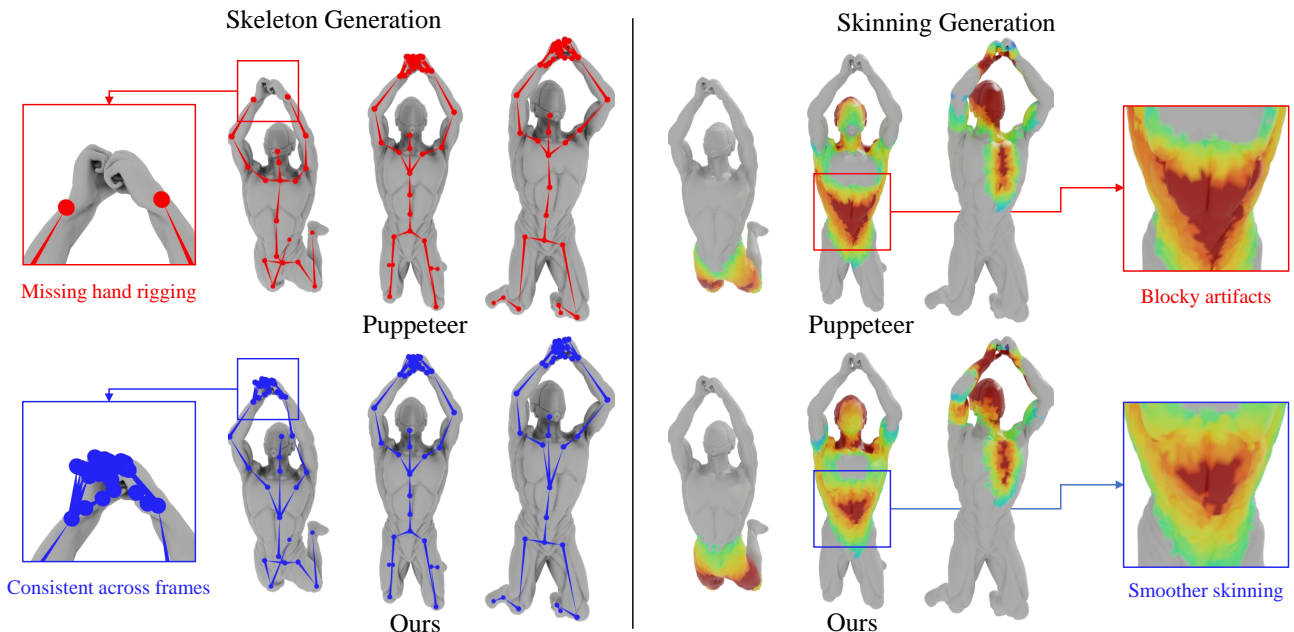


Figure 1. Our method (top, blue) yields a complete, temporally consistent skeleton with smooth, coherent skinning weights, whereas Puppeteer (bottom, red) [79] produces an incomplete skeleton with missing hand rigging and unstable, blocky skinning.

Abstract

State-of-the-art rigging methods assume a canonical rest pose—an assumption that fails for sequential data (e.g., animal motion capture or AIGC/video-derived mesh sequences) that lack the T-pose. Applied frame-by-frame, these methods are not pose-invariant and produce topological inconsistencies across frames. Thus We propose SPRig, a general fine-tuning framework that enforces cross-frame consistency losses to learn pose-invariant rigs on top of existing models. We validate our approach on rigging using a new permutation-invariant stability protocol. Experiments demonstrate SOTA temporal stability: our method produces coherent rigs from challenging sequences and dramatically reduces the artifacts that plague baseline methods. The code will be released publicly upon acceptance.

1. Introduction

3D character rigging, which encompasses skeleton generation [16] and skinning [47], is a fundamental, yet time-consuming bottleneck in modern content creation pipelines for games, film, and virtual reality [61]. Therefore, many automatic rigging tools [12, 21, 23, 36, 37, 48, 54, 55, 58, 68, 81, 83, 84, 108] have been developed to accelerate this process. Early automatic rigging methods like *Pinocchio* [8] relied on geometric heuristics and template fitting, which often struggle to generalize to diverse topologies. With the advent of deep learning [46], *RigNet* [101] pioneered the formulation of rigging as a learning task. More recently, state-of-the-art methods (SOTAs) have achieved significant boosts by using powerful Transformer-based [92] autoregressive models [73], such as *UniRig* [114] and *Puppeteer* [79], to generate high-quality

rigs.

However, these SOTA models are designed for static input, specifically a single T-pose. This assumption fails for modern animated sequences from text-to-4d model [4, 18, 24, 96, 110] or video reconstruction [19, 33, 53, 77, 87, 105, 120], which often lack a T-pose. When applied frame-by-frame, these models lack temporal awareness and fail to maintain consistency across the sequence. This failure manifests itself as severe visual artifacts, such as catastrophic topological flicker between frames (see Fig. 1).

The field also lacks robust metrics to evaluate temporal stability. Existing static rigging metrics like Joint Chamfer Distance [101] are designed to assess single-frame quality and are thus incapable of capturing this cross-frame instability. Traditional motion or video metrics [88] are insensitive to the *structural* and *topological* changes that are central to our problem.

Addressing temporal inconsistency is crucial. Rigs that flicker frame-to-frame are effectively unusable, as they disrupt downstream animation pipelines and require manual cleanup, negating the benefits of automation. Unlike the relative abundance of static rigging data [13, 23, 81, 89, 100, 114], high-quality labeled 4D datasets with skeletons and skinning are extremely rare. Consequently, the lack of large-scale 4D supervision forces us to extract a signal from the sequence itself. Our key insight builds on a fundamental assumption in computer graphics: an animated sequence represents a single object, which should therefore have a single, pose-invariant rig [32]. We operationalize it as a self-supervised [35] signal: a canonical rig derived from an anchor frame serves as a target to fine-tune the pre-trained model, enforcing consistency across the sequence.

Therefore, we propose *SPRig*, a novel fine-tuning framework that implements this strategy. *SPRig* injects temporal consistency into pre-trained static rigging models by leveraging self-supervised signals from unlabeled animated mesh sequences, improving the stability of state-of-the-art (SOTA) models and making them robust to pose variations.

Specifically, Our framework enforces temporal consistency by referencing a single anchor frame, typically the first frame. This single-anchor strategy is applied at two levels: (1) For skeleton estimation, token and geometric losses guide the Transformer to replicate the anchor’s canonical tokenization across all subsequent frames. (2) For skinning weight prediction, an articulation-invariant loss aligns all frames to a high-quality distribution derived from the same anchor. To address the evaluation gap, we further introduce a robust protocol of permutation-invariant metrics to accurately quantify temporal stability, an area currently lacking standardized measures.

In summary, our contributions are as follows.

- *SPRig*, a self-supervised fine-tuning framework that enhances temporal stability and pose-invariance in state-of-

the-art models using only unlabeled sequences.

- A set of dual consistency losses for learning pose-invariant skeleton topology and coherent skinning from temporal data.
- A robust, permutation-invariant evaluation protocol for benchmarking temporal stability, addressing a critical gap in rigging evaluation.

2. Related Work

Automatic rigging from static meshes. Early automatic rigging relied on geometric heuristics and template fitting [1, 3, 8, 11, 15, 30, 40, 66, 67, 69, 70, 85, 86, 103, 104]. These methods (e.g., *Pinocchio* [8]), depend strongly on template quality and struggle with novel topologies. To improve generalization, the field shifted to data-driven approaches. *RigNet* [101] framed rigging (skeleton + skinning) as an end-to-end learning problem, and subsequent models trained on large artist-created datasets [27, 28, 51, 116] showed strong generalization. With Transformers succeeding in 3D [52, 71, 95, 109, 111, 112, 118, 119], recent SOTAs adopt autoregressive sequence-generation frameworks (*UniRig* [114], *Puppeteer* [79]). These methods excel on static assets but are fundamentally non-temporal, which leads to frame-to-frame inconsistencies (e.g., joint drift, topology flicker) that we target in this work.

Rigging and motion analysis from dynamic sequences. A parallel line of research extracts rigging or motion directly from dynamic mesh sequences [2, 26, 38, 41, 45, 60, 65]. This direction aligns with the graphics view that a skeleton compactly represents deformation; recent advances extend to point-cloud and video-based reconstruction (*MoRig* [102], *LASR* [105], *Reacto* [78] and others [75, 80, 82, 94, 106, 107, 113, 120]). High-quality mesh sequences are increasingly obtainable (often reconstructed from in-the-wild video), but they are typically unlabeled. While unsuitable for supervised training, these unlabeled 4D sequences provide the perfect self-supervised signal exploited by *SPRig*.

Evaluating structural and topological consistency. Standard rigging metrics (e.g., Joint Chamfer Distance, Skinning LBS Error) are single-frame and thus blind to cross-frame drift or topological flicker [9, 14, 47, 59]. Temporal metrics from motion/video literature (e.g., Normalized Power Spectrum Similarity, Fréchet Video Distance) measure trajectory or pixel-distribution fidelity but not structural changes in a skeleton [34, 91]. General-purpose graph-similarity learners exist [6, 7, 17, 29, 31, 39, 49, 72, 74, 90, 93, 99, 117, 121], but they either require task-specific training or too generic. Other methods [5, 10, 20, 22, 56, 63, 64, 97, 98] do evaluate skeleton consistency, but they evaluate cross-species similarity or for 2D skeleton and trees only. Therefore, they needed some adaptation, we will discuss

about this later in the paper (See 5).

3. Skeleton Generation

Directly applying the autoregressive skeleton generator independently to each frame leads to severe re-parenting and token-level jitter. We instead align all frames to a canonical token sequence defined on an anchor frame, and complement this with pose- and permutation-invariant geometric regularization to learn a temporally consistent skeleton.

3.1. Backbone

Our framework is applied to fine-tune a pre-trained, causal auto-regressive decoder G_θ [73]. This backbone decoder is conditioned on per-frame features \mathbf{F}_k . The decoder G_θ generates a token stream $\hat{\mathbf{t}}_k = \{\hat{t}_i\}_{i=1}^L$, with the total L length of the token sequence, by factorizing the joint probability:

$$p_\theta(\hat{\mathbf{t}}_k | \mathbf{F}_k) = \prod_{i=1}^L p_\theta(\hat{t}_i | \hat{\mathbf{t}}_{<i}, \mathbf{F}_k). \quad (1)$$

This token stream $\hat{\mathbf{t}}_k = G_\theta(\mathbf{F}_k)$ jointly encodes geometry and topology by being grouped into quadruples (t_x, t_y, t_z, t_p) per joint. Here, $t_x, t_y, t_z \in \{1, \dots, n_{\text{disc}}\}$ are the integer bins of the quantized Cartesian coordinates (on $[-0.5, 0.5]$), and $t_p \in \{0, \dots, J\}$ is the discrete parent label, where $t_p=0$ denotes a root joint of a skeleton.

At inference, decoding this stream yields a skeleton $\hat{\mathcal{S}}_k = (\hat{\mathbf{X}}_k, \hat{\mathbf{p}}_k)$, containing the joints $\hat{\mathbf{X}}_k \in \mathbb{R}^{J \times 3}$ and the parent vector $\hat{\mathbf{p}}_k \in \{0, \dots, J\}^J$. For our fine-tuning objective, we set $k=0$ as the anchor frame.

3.2. Token-space (Transformer) consistency

Motivation. State-of-the-art autoregressive skeleton generators operate on 1D discrete token sequences that are extremely sensitive to small geometric perturbations, which is the main source of topological flicker. Our key insight is that the kinematic topology of a single object should be invariant to pose. We therefore encourage the model to learn a canonical tokenization in which all frames in a clip are mapped to the anchor frame’s token sequence.

Formulation. Our token-space loss has two terms: $\mathcal{L}_{\text{anchor}}$ is a self-supervised loss on the anchor frame itself, and \mathcal{L}_{KL} symmetrically aligns non-anchor frames to the anchor token sequence. Both terms are weighted cross-entropies in which parent tokens receive a larger weight ($\alpha > 1$) so that the discrete topology is stabilized first. See Supplementary Material for full definition.

The overall token-space objective is

$$\mathcal{L}_{\text{token}} = \lambda_{\text{anchor}} \mathcal{L}_{\text{anchor}} + \lambda_{\text{sym}} \mathcal{L}_{\text{KL}}, \quad (2)$$

with weights $\lambda_{\text{anchor}}, \lambda_{\text{sym}} > 0$. Note that we use explicit coefficients for both terms for semantic clarity, although we

note that only their relative ratio is significant to the optimization.

The token-space objective treats the anchor frame as a canonical discrete skeleton and forces all other frames in the clip to be encoded with the same token sequence. We apply teacher-forced autoregressive cross-entropy on the anchor and a symmetric variant on non-anchor frames that conditions on their point-cloud features but still predicts the anchor tokens. Within each (t_x, t_y, t_z, t_p) group we up-weight the parent slot by a factor $\alpha > 1$ so that the discrete topology is stabilized before joint locations. This encourages a pose-invariant canonical tokenization for each sequence; the exact form of the anchor and symmetric losses is given in the supplementary material.

3.3. Geometry-space (permutation-invariant) consistency

Motivation. Token-space supervision alone is insufficient, because it still suffers from exposure bias at inference time. We therefore introduce a complementary geometry-space loss $\mathcal{L}_{\text{geom}}$ as a robust regularizer that is explicitly invariant to both pose changes and joint permutations.

Formulation. This loss first removes global rigid motion by aligning the skeletons (either via structure tensors [44] or standard Procrustes analysis [76]) so that large-scale bone arrangements are comparable across frames. It then measures permutation-invariant discrepancies in the aligned space by comparing bone directions \mathcal{L}_{dir} , bone-length distributions \mathcal{L}_{len} , and joint endpoints \mathcal{L}_{ch} between each frame and the anchor. See Suppl. for the details.

We average aligned distances over non-anchor frames and use the three criteria:

$$\mathcal{L}_{\text{geom}} = \frac{1}{K-1} \sum_{k=1}^{K-1} \left(\lambda_{\text{dir}} \mathcal{L}_{\text{dir}} + \lambda_{\text{len}} \mathcal{L}_{\text{len}} + \lambda_{\text{ch}} \mathcal{L}_{\text{ch}} \right). \quad (3)$$

We defer exact number of $\lambda_{\text{dir}}, \lambda_{\text{len}}, \lambda_{\text{ch}}$ to the supplementary material.

The geometry-space loss operates on decoded skeletons at inference time and complements token-space supervision. We first remove global rigid motion by aligning each predicted frame to the anchor (via a structure-tensor or Procrustes-based rigid alignment), so that only articulated motion remains. On the aligned skeletons we use three permutation-invariant criteria: a bidirectional nearest-neighbor penalty on edge directions, a discrepancy between sorted bone-length spectra, and a symmetric Chamfer distance between edge endpoints. These terms penalize geometric jitter and structural drift while being insensitive to joint permutations; full expressions are deferred to the supplementary material.

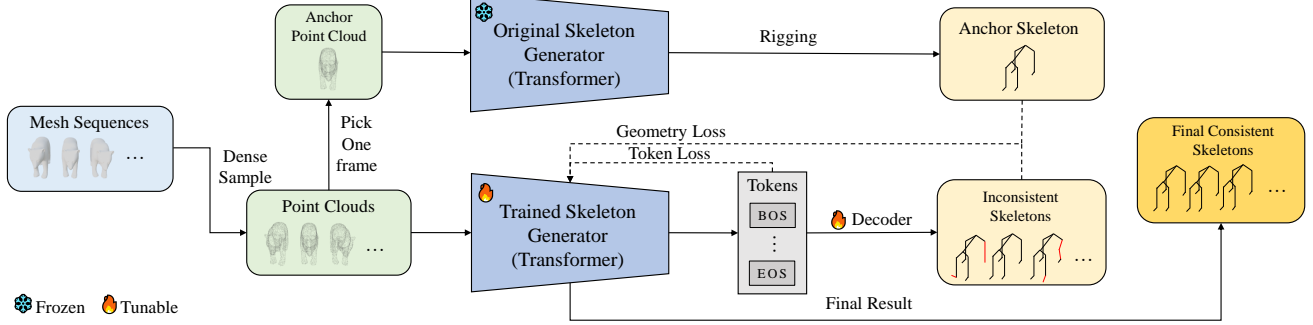


Figure 2. **Skeleton generation overview.** Point clouds sampled from mesh sequences are fed to a Transformer-based skeleton generator. An anchor skeleton from the original generator defines a canonical target; token-space and geometry-space consistency losses fine-tune the model so that decoded tokens yield temporally consistent skeletons.

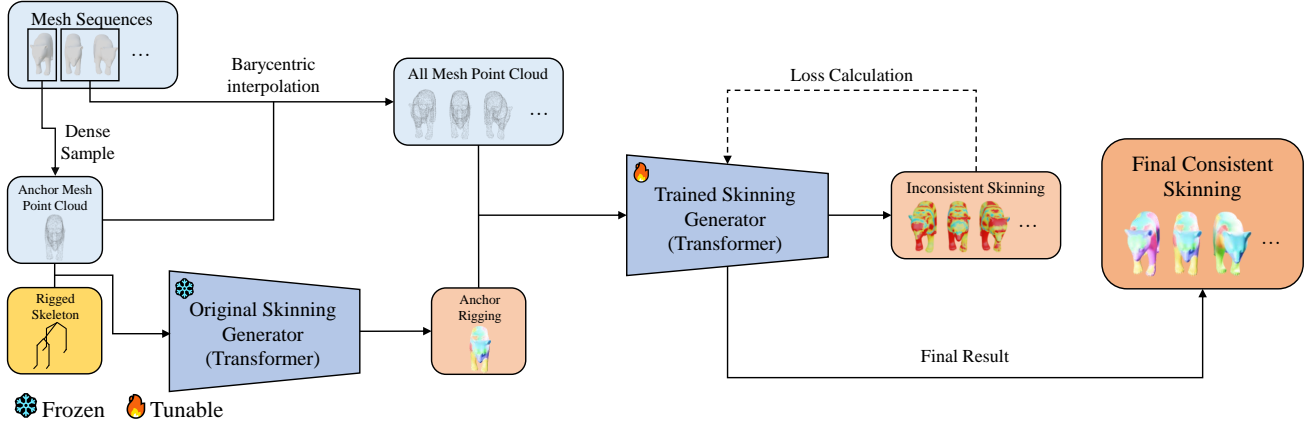


Figure 3. **Skinning generation pipeline overview.** A high-quality anchor teacher is first generated using a pretrained generator on the anchor frame. Pose-consistent query points are sampled from the full mesh sequence via barycentric interpolation. A skinning generator is then fine-tuned: its predictions on all query points are compared against the single anchor teacher using our articulation-invariant consistency loss, forcing the model to learn a pose-invariant mapping and produce temporally consistent skinning.

3.4. Overall objective

The total objective is $\mathcal{L}_{\text{total}} = \lambda_{\text{token}} \mathcal{L}_{\text{token}} + \lambda_{\text{geom}} \mathcal{L}_{\text{geom}}$. This formulation cleanly separates token-space learning of a frame-invariant canonical mapping ($\mathcal{L}_{\text{token}}$) from geometry-space regularization for robust inference ($\mathcal{L}_{\text{geom}}$).

4. Skinning Generation

Setup. Given an animated mesh sequence $\mathcal{M} = \{\mathbf{M}_k\}_{k=0}^K$ with consistent topology, we choose the first frame, $k=0$, as the *anchor*, and normalize all geometry using the anchor’s axis-aligned bounding box. We sample N surface points on \mathbf{M}_0 by triangle-area importance sampling. Sharing the same sampling index on every frame k in the sequence, we form a per-frame query matrix $\mathbf{U}_k \in \mathbb{R}^{N \times 6}$, concatenated by the (anchor-normalized) position $\mathbf{e}_k \in \mathbb{R}^{N \times 3}$ and the unit-length normal $\mathbf{n}_k \in \mathbb{R}^{N \times 3}$ along the feature dimension. Let $\mathbf{X} \in \mathbb{R}^{J \times 3}$ be the anchor-normalized joint co-

ordinates, and $\mathbf{p} \in \{0, \dots, J\}^J$ the parent indices (root self-parented). We use a valid joint mask $\mathbf{V} \in \{0, 1\}^J$, where $\mathbf{V}_j = 1$ if and only if joint j is a valid (non-padding) joint, and $\mathbf{V}_j = 0$ otherwise. From \mathbf{p} we induce unweighted shortest-path distances on the joint tree, forming $\mathbf{D} \in \mathbb{R}^{J \times J}$. Under consistent topology, \mathbf{p} , \mathbf{V} , and \mathbf{D} are frame-invariant; \mathbf{X} is normalized and shared across frames.

4.1. Backbone

Let H_ϕ be any differentiable predictor that, given per-frame query data \mathbf{U}_k together with compact skeletal codes $(\mathbf{X}, \mathbf{p}, \mathbf{V}, \mathbf{D})$ —anchor-normalized joint positions, parent indices, a valid-joint mask, and joint-tree distances—outputs per-point distributions over joints:

$$\hat{\mathbf{W}}_k = H_\phi(\mathbf{U}_k; \mathbf{X}, \mathbf{p}, \mathbf{V}, \mathbf{D}), \quad (4)$$

where the matrix $\hat{\mathbf{W}}_k \in \mathbb{R}^{N \times J}$ is row-stochastic ($\hat{\mathbf{W}}_k[i, :] \in \Delta^{J-1}$). In experiments, we instantiate H_ϕ with a tri-stream transformer (Point/Joint/Shape) and a lightweight

topology-aware joint attention. See supplementary material for details.

4.2. Anchor teacher via barycentric transfer

We adopt a high-fidelity pretrained predictor on the anchor vertices $\mathbf{V}_{\text{vtx}}^{(0)} \in \mathbb{R}^{N_v \times 3}$ of \mathbf{M}_0 to obtain a vertex teacher $\mathbf{W}_{\text{vtx}}^T \in \mathbb{R}^{N_v \times J}$ (zero for invalid joints). With the sampled face index f_i (with vertices $(\mathbf{v}_{f_i,1}^{(k)}, \mathbf{v}_{f_i,2}^{(k)}, \mathbf{v}_{f_i,3}^{(k)})$) and barycentric weights λ_i , we transfer supervision to queries by barycentric interpolation on the anchor:

$$\mathbf{e}_i^{(0)} = \sum_{r=1}^3 \lambda_{i,r} \mathbf{v}_{f_i,r}^{(0)}, \quad (5)$$

$$\mathbf{W}_{i,:}^T = \sum_{r=1}^3 \lambda_{i,r} (\mathbf{W}_{\text{vtx}}^T)_{f_i,r,:}. \quad (6)$$

The point teacher $\mathbf{W}^T \in \mathbb{R}^{N \times J}$ is shared across all frames and served as the canonical, pose-invariant target. To suppress noise in the teacher signal, we apply a Top- K_s truncation to \mathbf{W}^T and use a custom renormalization operator $\mathcal{R}(\cdot, \mathbf{m})$ together with a masked averaging operator $\langle \cdot, \mathbf{m} \rangle$. See Supplementary Material for full information.

For skinning, we construct a high-quality vertex-level teacher on the anchor mesh and transfer it to sampled surface points via barycentric interpolation of their three incident vertices, producing a dense, pose-invariant target shared across all frames. To suppress noise from small teacher weights, we build a per-point Top- K_s mask that retains the most influential valid joints, down-weights the remaining valid joints, and discards invalid ones. Teacher and predicted weights are then renormalized on this masked support, ensuring that the loss emphasizes the joints relevant to each query point. The exact masked operators are provided in the supplementary material.

4.3. Loss: articulation-invariant consistency with geometric prior

Our total loss consists of two parts. The first is a consistency distillation loss $\mathcal{L}_{\text{cons}}$, which uses a symmetric KL divergence term \mathcal{L}_{KL} and an L1 term \mathcal{L}_1 to pull predictions on all non-anchor frames toward the anchor teacher \mathbf{W}^T , together with an anchor-frame loss $\mathcal{L}_{\text{anchor}}$ that prevents the teacher from drifting. The second part is a structural regularization loss \mathcal{L}_{reg} , which includes an entropy loss \mathcal{L}_{ent} encouraging sparse, confident assignments, and a geometric prior loss $\mathcal{L}_{\text{prior}}$ that biases weights toward nearby bones. Finally, the overall skinning objective is

$$\mathcal{L}_{\text{total}} = \mathcal{L}_{\text{cons}} + \mathcal{L}_{\text{reg}}. \quad (7)$$

Concretely, $\mathcal{L}_{\text{cons}}$ averages, over all non-anchor frames and query points, a *masked symmetric* KL divergence and

Table 1. **Temporal Stability (top) and Static Generation Quality (bottom).** Our method reduces geometric jitter (PJDD) by $25\times$ over the Puppeteer baseline, and also improves static alignment on Articulation-XL ν 2. Metrics marked with (↓) are lower-better; JAD and MPJPE@Anchor are diagnostic.

Model	Temporal Stability				
	PJDD (↓)	BLRD (↓)	GSD (↓)	JAD (diag.)	MPJPE@Anchor (diag.)
Puppeteer	17.46	34.37	0.062	0.343	0.592
Ours	0.68	17.74	0.056	0.380	0.731
Static Generation Quality (Articulation-XL ν 2)					
Model	CD-J2J (↓)	CD-J2B (↓)	CD-B2B (↓)		
Puppeteer	0.0311	0.0237	0.0198		
Ours	0.0270	0.0213	0.0188		

a *masked* L_1 distance between the predicted joint-weight distributions and the anchor teacher; the additional $\mathcal{L}_{\text{anchor}}$ term applies the same discrepancy on the anchor frame so that the student does not drift away from its teacher during fine-tuning. The regularization term \mathcal{L}_{reg} combines a masked Shannon-entropy penalty, which discourages overly diffuse (high-entropy) weights, with a geometric prior that turns point-to-bone distances into a soft probability distribution and penalizes deviations from this distance-based prior, thereby biasing mass toward nearby bones. We use scalar weights to balance the five components \mathcal{L}_{KL} , \mathcal{L}_1 , $\mathcal{L}_{\text{anchor}}$, \mathcal{L}_{ent} , and $\mathcal{L}_{\text{prior}}$; full formulas and hyperparameters are given in the supplementary material.

Intuitively, this articulation-invariant objective distills the anchor-frame teacher into the student across time: for non-anchor frames, masked symmetric KL and masked L_1 terms pull the predicted joint-weight distributions toward the anchor teacher, while the entropy and geometric-prior regularizers encourage sparse, confident predictions that place most mass on bones that are geometrically close to each query point.

5. Experiment

5.1. Skeleton Generation

Datasets and Preprocessing. We use dynamic sequences from the DeformingThings4D (DT4D) [50] dataset. A validation set of 125 sequences is defined, with the remaining sequences used for training. Fine-tuning requires no additional manual annotations. Training data are constructed in a self-supervised manner: (1) the pre-trained baseline model (Puppeteer) generates an anchor rig $(\hat{\mathcal{S}}_0, \hat{\mathbf{p}}_0)$ for the first frame ($k = 0$); (2) the rig is encoded into a canonical token sequence \mathbf{t}_0 ; and (3) 6D point clouds (XYZ + normals) are sampled from the first three frames ($k = 3$). Each training sample thus consists of these point clouds and the corresponding anchor token sequence \mathbf{t}_0 .

Evaluation Metrics. To evaluate temporal stability, we introduce a robust protocol of permutation-invariant metrics. These include Pairwise Joint Distance Deviation (PJDD)

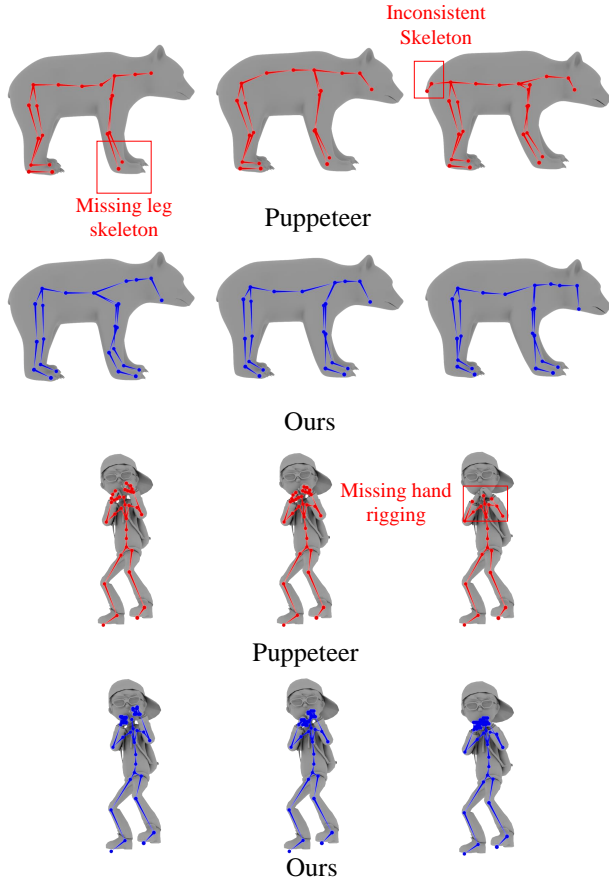


Figure 4. Qualitative comparison of skeleton predictions on non-humanoid (**Bear**, left) and humanoid (**Human**, right) meshes. Top row (blue): our method produces temporally stable and complete skeletons across frames. Bottom row (red): the Puppeteer baseline often misses or distorts structures (e.g., missing leg skeletons on the bear and missing hand rigging on the human), and exhibits inconsistent skeleton topology between frames (red boxes).

and Bone Length Relative Deviation (BLRD) to measure geometric jitter, and Graph Spectral Discrepancy (GSD) to assess structural consistency. We also use Joint Angle Discrepancy (JAD) and MPJPE@Anchor as diagnostics. For static quality, we follow prior work and use Chamfer Distance (CD-J2J, CD-J2B, CD-B2B). A complete and detailed description of all metrics, including both intuitive explanations and their full mathematical formulations, is provided in the supplementary material (Sec. 10).

Implementation Details. We fine-tune the SkeletonGPT (Puppeteer) backbone. Complete details on the training setup, optimizer, training hardware, and all hyperparameters are deferred to the supplementary material. See Sec. 9.

Temporal Stability. We compare our full model (Ours) against the pre-trained Puppeteer baseline on temporal stability (Tab. 1). The baseline exhibits poor temporal stabil-

ity, with high PJDD (17.46) and BLRD (34.37), indicating chaotic geometric and topological predictions. Our method dramatically improves performance, reducing PJDD over $25 \times$ ($17.46 \rightarrow 0.68$) and halving BLRD, demonstrating that the dual-consistency loss effectively mitigates symbolic brittleness. The JAD metric remains comparable (0.34 vs 0.38), confirming that our model preserves realistic angular motion without “freezing” the skeleton

Static Generation Quality. A key concern with fine-tuning is catastrophic forgetting [43, 62]. We evaluate our model on the original Articulation-XLV2 benchmark (Tab. 1) and find that performance is not only preserved but improved, surpassing the Puppeteer baseline across all standard static metrics. The slight increase in MPJPE@Anchor (0.73 vs 0.59) (Tab. 1) does not indicate reduced accuracy; it reflects the model’s divergence from the baseline’s sub-optimal pseudo-labels. Superior CD-J2J/B2B scores confirm that our model achieves both higher temporal stability and greater fidelity to ground-truth static skeletons.

Ablation Study. We conduct an ablation study on the temporal stability task (Tab. 2). Our dual-consistency framework is highly synergistic. Removing either the geometric loss ($\mathcal{L}_{\text{geom}}$, Ablation (1)) or the token-space loss ($\mathcal{L}_{\text{token}}$, Ablation (2)) severely degrades PJDD by +102% and +76%, respectively, confirming the necessity of both the topological anchor ($\mathcal{L}_{\text{token}}$) and the geometric constraint ($\mathcal{L}_{\text{geom}}$). The most notable result is Ablation (3): reducing the parent-token weight α from 3.0 to 1.0 (reverting WCE to standard CE) worsens PJDD by 100% and BLRD by 55%, validating that stabilizing the symbolic topology (t_p) is crucial for achieving temporal-geometric stability.

Table 2. Ablation study on temporal stability. All components are critical. Removing the parent-token weighting ($\alpha = 1$) causes a catastrophic failure in both PJDD and BLRD.

Model	PJDD (\downarrow)	BLRD (\downarrow)	GSD (\downarrow)
Ours (Full)	0.68	17.7	0.056
(1) w/o $\mathcal{L}_{\text{geom}}$	1.38	18.4	0.067
(2) w/o $\mathcal{L}_{\text{token}}$	1.20	18.7	0.047
(3) w/o Parent Weight ($\alpha = 1$)	1.36	27.5	0.073

5.2. Skinning Generation

Implementation Details. We conduct experiments on the DT4D dataset and fine-tune the pretrained Puppeteer skinning backbone. All implementation details are detailed in the supplementary material. See Sec. 12.

Metrics. We evaluate performance using two categories of metrics. For *temporal consistency*, we adopt three measures: (1) $L_1(B, C \rightarrow A)$ (L1 Error), which quantifies the L1 distance between perturbed-frame predictions $\hat{\mathbf{W}}^{(k)}$ and the anchor-frame teacher \mathbf{W}^T (lower is better); (2) $SymKL(B, C \leftrightarrow A)$ (SymKL Div.), which measures shape consistency between predicted distributions (lower

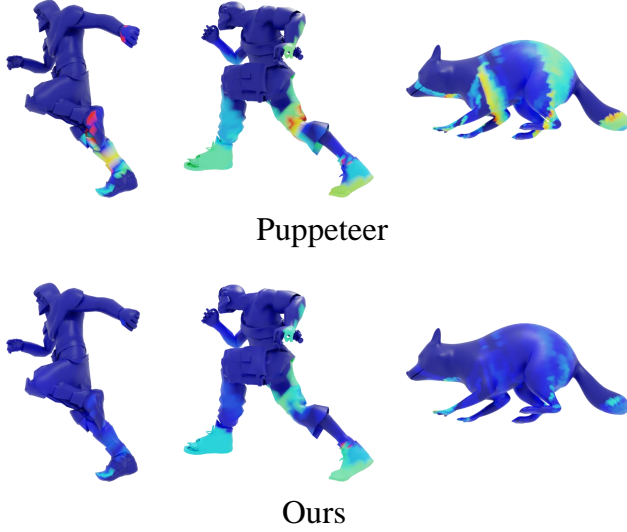


Figure 5. Qualitative comparison of temporal consistency

(L1 Error Heatmap). We visualize the per-vertex L_1 error ($L_1(\hat{\mathbf{W}}^{(k)}, \mathbf{W}^T)$) between the prediction on a perturbed frame and the static anchor teacher \mathbf{W}^T . The colormap ranges from blue (zero error) to red (high error). **(Left - Puppeteer):** The baseline model exhibits severe temporal inconsistency, with large high-error regions on the limbs. **(Right - Ours):** Our fine-tuning framework almost completely eliminates this inconsistency. The high-error regions are suppressed, and the surfaces remain dark blue, visually confirming the quantitative gains in Table 3.

is better); and (3) Entropy, which evaluates the sharpness of the predicted distributions, with lower values indicating more confident predictions. Detailed explanation for temporal consistency metrics are deferred to supplementary material (See 13). For *static quality*, we follow the Puppeteer’s evaluation protocol and report Precision, Recall, and average L1 on the Articulation-XL, Diverse-pose, and ModelsResource benchmarks.

Temporal consistency. We assess temporal coherence by comparing our fully fine-tuned model (50 epochs) with the pretrained Puppeteer baseline. As shown in Tab. 3, our framework achieves a 30.3% reduction in L_1 consistency error ($1328.80 \rightarrow 925.77$) and a notable 51.3% reduction in the key temporal stability metric $SymKL$ ($2226.63 \rightarrow 1084.71$). These results confirm that our fine-tuning effectively incorporates the pose-invariance prior into the model.

Table 3. Temporal consistency comparison. our fine-tuning substantially improves temporal stability.

Method	$L_1(B, C \rightarrow A) \downarrow$	$SymKL(B, C \leftrightarrow A) \downarrow$	Entropy(diag.)
Puppeteer	1328.80	2226.63	1368.45
Ours	925.77	1084.71	1396.95
Improvement	30.3%	51.3%	-

Static Quality Analysis. We examine whether improving temporal consistency harms static prediction quality by

comparing the fine-tuned model to the baseline on three standard benchmarks (see Tab. 4). Results show a modest trade-off: optimizing for temporal consistency yields small wins and losses on static metrics. On Diverse-pose the fine-tuned model improves across all metrics ($L_1: 0.405 \rightarrow 0.378$). On ModelsResource [89, 100] Recall increases substantially ($0.816 \rightarrow 0.883$) at the expense of Precision. On Articulation-XL the baseline holds a slight advantage in Precision and L_1 . Overall, these minor static changes are acceptable given the large temporal-consistency gains (see Tab. 3) The fine-tuned model maintains comparable static performance, and improved a lot in the Diverse-pose dataset, which further indicates that our model handles provides better capability on meshes in different poses.

Table 4. Static Prediction Quality comparison on standard benchmarks. Results show a nuanced trade-off, where our fine-tuned model maintains comparable or superior performance on average, preserving static quality while gaining temporal stability.

Method	Benchmark	Precision \uparrow	Recall \uparrow	Avg. L1 Dist. \downarrow
Puppeteer	Articulation-XL	0.876	0.740	0.335
	Diverse-pose	0.836	0.722	0.405
	ModelsResource	0.797	0.816	0.443
Ours	Articulation-XL	0.863	0.745	0.355
	Diverse-pose	0.842	0.734	0.378
	ModelsResource	0.732	0.883	0.462

Ablation Study. To validate the necessity of each component in our loss function (Eq. 7), we conduct a series of ablation experiments. We use our full model trained for 12 epochs as the control group and individually remove each of the five loss terms.

Table 5. Ablation study of the loss components (all models trained for 12 epochs). The catastrophic failure in all ablation cases demonstrates that all five components are necessary.

Model (Component Removed)	$L_1(B, C \rightarrow A) \downarrow$	$SymKL(B, C \leftrightarrow A) \downarrow$	Status
Full Model (12e)	982.35	1071.48	Converged
<i>For reference:</i>			
Puppeteer (Baseline)	1328.80	2226.63	-
<i>Ablations:</i>			
w/o \mathcal{L}_{sym} (SymKL)	3904.10	19740.44	Failure
w/o \mathcal{L}_1 (L1)	4018.83	17964.26	Failure
w/o \mathcal{L}_{anchor} (Anchor)	4018.23	17556.14	Failure
w/o \mathcal{L}_{ent} (Entropy)	4018.80	17964.15	Failure
w/o \mathcal{L}_{prior} (Prior)	4018.76	17957.60	Failure

The results in Table 5 clearly demonstrate the necessity of our loss design. All components are critical: Removing any one of the five loss components results in a catastrophic failure of the training. The L_1 error (e.g., $\approx 3900 - 4000$) and $SymKL$ divergence ($\approx 17000 - 19000$) degrade sharply, performing not only far worse than our full model ($L_1 = 982$), but also significantly worse than the pretrained Puppeteer baseline ($L_1 = 1328$). The core distillation terms (\mathcal{L}_{sym} and \mathcal{L}_1) and the stabilizers (\mathcal{L}_{anchor} , \mathcal{L}_{ent} , and \mathcal{L}_{prior}) act as crucial stabilizers. Removing any one of these leads to training collapse, proving that while \mathcal{L}_{sym} and

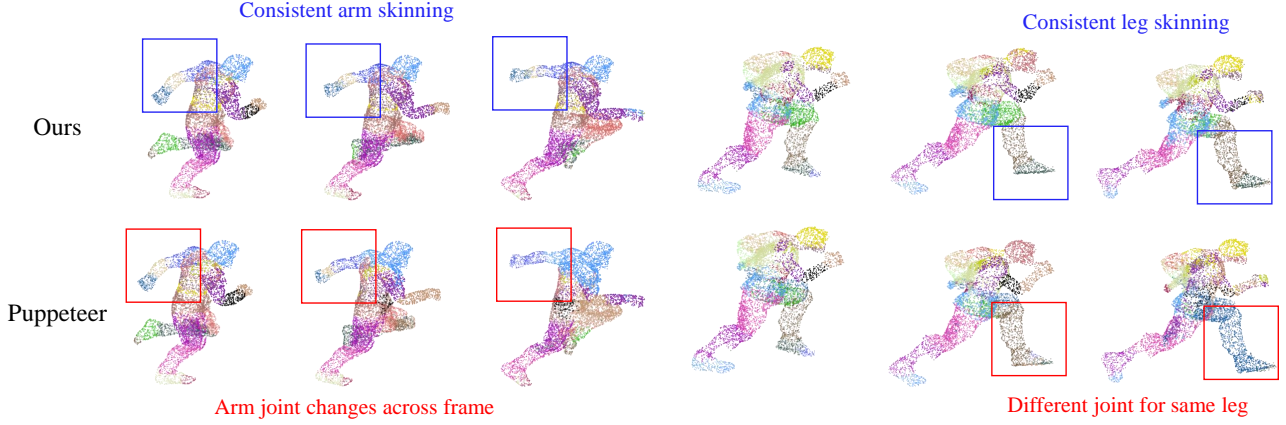


Figure 6. **Qualitative comparison of skinning generation** on running human sequences from the DT4D dataset. The visualization colors each point based on the joint with the maximum skinning weight influence (one color per joint). **Ours** (Top row) produces temporally consistent skinning assignments for both the arms and legs across all frames, as highlighted by the blue boxes. In contrast, the **Puppeteer baseline** (Bottom row) exhibits significant temporal instability. The joint assignments flicker between frames, showing inconsistent colors for the arm (red box, left) and the same leg (red box, right).

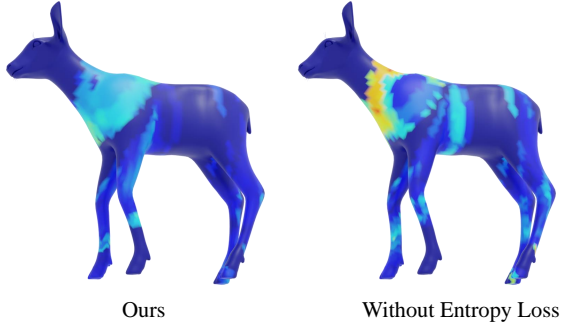


Figure 7. **Ablation of entropy regularization.** We visualize the per-vertex Shannon entropy of predicted skinning weights \hat{W} (blue: low entropy, sparse and sharp; red: high entropy, blurry and diffuse). **Left:** the full model with \mathcal{L}_{ent} yields low-entropy, unambiguous assignments. **Right:** removing \mathcal{L}_{ent} produces large high-entropy regions and uncertain weights, consistent with the degradation reported in Table 5.

\mathcal{L}_1 provide the primary learning signal, the training cannot converge to a meaningful solution without the three regularization terms constraining the optimization space. The five components of \mathcal{L}_{total} thus form a tightly-coupled and indispensable system, working in concert to enable the model to stably learn temporally-consistent skinning weights.

6. Discussion

Our work brings a new perspective to the data-driven model articulation domain by introducing unlabeled mesh sequences as a source of training data. We propose a general fine-tuning framework that specifically addresses the severe temporal inconsistencies arising when state-of-the-

art (SOTA) static rigging models are applied to animated sequences that lack a canonical rest pose.

This framework leverages the sequence’s inherent dynamic information:

1. **For skeleton generation**, we devised **token-space** and **geometry-space** consistency losses, compelling the Transformer model to learn a pose-invariant canonical tokenization and topology.
2. **For skinning weights**, we employed an **articulation-invariant** distillation loss, aligning predictions from all frames to a fixed “teacher” distribution generated from an anchor frame.

We also introduced a new suite of robust evaluation metrics to specifically quantify temporal stability. Experiments demonstrate that our method achieves SOTA temporal stability on both skeleton and skinning tasks. Critically, this stability is achieved while maintaining or even improving the model’s original static generation quality.

This work effectively cures the inconsistency of SOTA models when processing real-world data from AIGC or video capture, providing a more robust and reliable tool for automated content creation pipelines.

Looking ahead, our framework opens the door to several research directions. For example, one could explore fine-tuning on longer mesh sequences to capture more complex dynamics and further enhance long-term temporal consistency.

We also believe that leveraging mesh deformation as a rich supervisory signal for learning rigging holds immense potential, since 4D deformation provide far more information than single frame data. We hope this work serves as a first step in that direction and inspires further research on deformation-driven rigging.

References

[1] Nina Amenta and Marshall Bern. Surface reconstruction by voronoi filtering. In *Proceedings of the fourteenth annual symposium on Computational geometry*, pages 39–48, 1998. 2

[2] Dragomir Anguelov, Praveen Srinivasan, Daphne Koller, Sebastian Thrun, Jim Rodgers, and James Davis. Scape: shape completion and animation of people. In *ACM Siggraph 2005 Papers*, pages 408–416. 2005. 2

[3] Oscar Kin-Chung Au, Chiew-Lan Tai, Hung-Kuo Chu, Daniel Cohen-Or, and Tong-Yee Lee. Skeleton extraction by mesh contraction. *ACM transactions on graphics (TOG)*, 27(3):1–10, 2008. 2

[4] Sherwin Bahmani, Xian Liu, Wang Yifan, Ivan Skorokhodov, Victor Rong, Ziwei Liu, Xihui Liu, Jeong Joon Park, Sergey Tulyakov, Gordon Wetzstein, et al. Tc4d: Trajectory-conditioned text-to-4d generation. In *European Conference on Computer Vision*, pages 53–72. Springer, 2024. 2

[5] Xiang Bai and Longin Jan Latecki. Path similarity skeleton graph matching. *IEEE transactions on pattern analysis and machine intelligence*, 30(7):1282–1292, 2008. 2

[6] Yunsheng Bai, Hao Ding, Song Bian, Ting Chen, Yizhou Sun, and Wei Wang. Simgnn: A neural network approach to fast graph similarity computation. In *Proceedings of the twelfth ACM international conference on web search and data mining*, pages 384–392, 2019. 2

[7] Yunsheng Bai, Hao Ding, Ken Gu, Yizhou Sun, and Wei Wang. Learning-based efficient graph similarity computation via multi-scale convolutional set matching. In *Proceedings of the AAAI conference on artificial intelligence*, pages 3219–3226, 2020. 2

[8] Ilya Baran and Jovan Popović. Automatic rigging and animation of 3d characters. *ACM Transactions on graphics (TOG)*, 26(3):72–es, 2007. 1, 2

[9] Harry G Barrow, Jay M Tenenbaum, Robert C Bolles, and Helen C Wolf. Parametric correspondence and chamfer matching: Two new techniques for image matching. Technical report, 1977. 2

[10] Martin Bauer, Facundo MĂŠmoli, Tom Needham, and Mao Nishino. The z-gromov-wasserstein distance. *arXiv preprint arXiv:2408.08233*, 2024. 2

[11] Zeeshan Bhati, Asadullah Shah, Ahmad Waqas, and Hafiz Abid Mahmood Malik. Template based procedural rigging of quadrupeds with custom manipulators. In *2013 International Conference on Advanced Computer Science Applications and Technologies*, pages 259–264. IEEE, 2013. 2

[12] Shaojun Bian, Anzong Zheng, Ehtzaz Chaudhry, Lihua You, and Jian J Zhang. Automatic generation of dynamic skin deformation for animated characters. *Symmetry*, 10(4):89, 2018. 1

[13] Sue Blackman. Rigging with mixamo. In *Unity for Absolute Beginners*, pages 565–573. Springer, 2014. 2

[14] Gunilla Borgefors. Hierarchical chamfer matching: A parametric edge matching algorithm. *IEEE Transactions on pattern analysis and machine intelligence*, 10(6):849–865, 2002. 2

[15] Junjie Cao, Andrea Tagliasacchi, Matt Olson, Hao Zhang, and Zhinxun Su. Point cloud skeletons via laplacian based contraction. In *2010 Shape Modeling International Conference*, pages 187–197. IEEE, 2010. 2

[16] John E Chadwick, David R Haumann, and Richard E Parent. Layered construction for deformable animated characters. *ACM Siggraph Computer Graphics*, 23(3):243–252, 1989. 1

[17] Gary Chartrand, Grzegorz Kubicki, and Michelle Schultz. Graph similarity and distance in graphs. *Aequationes Mathematicae*, 55(1):129–145, 1998. 2

[18] Ce Chen, Shaoli Huang, Xuelin Chen, Guangyi Chen, Xiaoguang Han, Kun Zhang, and Mingming Gong. Ct4d: Consistent text-to-4d generation with animatable meshes. *arXiv preprint arXiv:2408.08342*, 2024. 2

[19] Jianqi Chen, Biao Zhang, Xiangjun Tang, and Peter Wonka. V2m4: 4d mesh animation reconstruction from a single monocular video. *CoRR*, 2025. 2

[20] Xin Chen, Jingbin Hao, Hao Liu, Zhengtong Han, and Shengping Ye. Research on similarity measurements of 3d models based on skeleton trees. *Computers*, 6(2):17, 2017. 2

[21] Xu Chen, Yufeng Zheng, Michael J Black, Otmar Hilliges, and Andreas Geiger. Snarf: Differentiable forward skinning for animating non-rigid neural implicit shapes. In *Proceedings of the IEEE/CVF International Conference on Computer Vision*, pages 11594–11604, 2021. 1

[22] Samir Chowdhury and Facundo Mémoli. The gromov-wasserstein distance between networks and stable network invariants. *Information and Inference: A Journal of the IMA*, 8(4):757–787, 2019. 2

[23] Zedong Chu, Feng Xiong, Meiduo Liu, Jinzhi Zhang, Mingqi Shao, Zhaoxu Sun, Di Wang, and Mu Xu. Humanrig: Learning automatic rigging for humanoid character in a large scale dataset. In *Proceedings of the Computer Vision and Pattern Recognition Conference*, pages 304–313, 2025. 1, 2

[24] Sisi Dai, Xinxin Su, Boyan Wan, Ruizhen Hu, and Kai Xu. Textmesh4d: High-quality text-to-4d mesh generation. *arXiv preprint arXiv:2506.24121*, 2025. 2

[25] Michael Dawson-Haggerty, Jordan Bacher, Alice Brown-Bivins, Christopher Forest, and Jason O’Kane. trimesh: Load and analyze triangular meshes. <https://trimesh.org/>, 2019. 2

[26] Edilson De Aguiar, Christian Theobalt, Sebastian Thrun, and Hans-Peter Seidel. Automatic conversion of mesh animations into skeleton-based animations. In *Computer Graphics Forum*, pages 389–397. Wiley Online Library, 2008. 2

[27] Matt Deitke, Ruoshi Liu, Matthew Wallingford, Huong Ngo, Oscar Michel, Aditya Kusupati, Alan Fan, Christian Laforte, Vikram Voleti, Samir Yitzhak Gadre, et al. Objaverse-xl: A universe of 10m+ 3d objects. *Advances in Neural Information Processing Systems*, 36:35799–35813, 2023. 2

[28] Matt Deitke, Dustin Schwenk, Jordi Salvador, Luca Weihs, Oscar Michel, Eli VanderBilt, Ludwig Schmidt, Kiana Ehsani, Aniruddha Kembhavi, and Ali Farhadi. Objaverse: A universe of annotated 3d objects. In *Proceedings of the IEEE/CVF conference on computer vision and pattern recognition*, pages 13142–13153, 2023. 2

[29] Cees H Elzinga and Hui Wang. Kernels for acyclic digraphs. *Pattern Recognition Letters*, 33(16):2239–2244, 2012. 2

[30] Andrew Feng, Dan Casas, and Ari Shapiro. Avatar reshaping and automatic rigging using a deformable model. In *Proceedings of the 8th ACM SIGGRAPH Conference on Motion in Games*, pages 57–64, 2015. 2

[31] Xinbo Gao, Bing Xiao, Dacheng Tao, and Xuelong Li. A survey of graph edit distance. *Pattern Analysis and applications*, 13(1):113–129, 2010. 2

[32] Michael Girard and Anthony A Maciejewski. Computational modeling for the computer animation of legged figures. *ACM SIGGRAPH Computer Graphics*, 19(3):263–270, 1985. 2

[33] Shubham Goel, Georgios Pavlakos, Jathushan Rajasegaran, Angjoo Kanazawa, and Jitendra Malik. Humans in 4d: Reconstructing and tracking humans with transformers. In *Proceedings of the IEEE/CVF International Conference on Computer Vision*, pages 14783–14794, 2023. 2

[34] Anand Gopalakrishnan, Ankur Mali, Dan Kifer, Lee Giles, and Alexander G Ororbia. A neural temporal model for human motion prediction. In *Proceedings of the IEEE/CVF Conference on Computer Vision and Pattern Recognition*, pages 12116–12125, 2019. 2

[35] Jie Gui, Tuo Chen, Jing Zhang, Qiong Cao, Zhenan Sun, Hao Luo, and Dacheng Tao. A survey on self-supervised learning: Algorithms, applications, and future trends. *IEEE Transactions on Pattern Analysis and Machine Intelligence*, 46(12):9052–9071, 2024. 2

[36] Zhiyang Guo, Jinxu Xiang, Kai Ma, Wengang Zhou, Houqiang Li, and Ran Zhang. Make-it-animatable: An efficient framework for authoring animation-ready 3d characters. In *Proceedings of the Computer Vision and Pattern Recognition Conference*, pages 10783–10792, 2025. 1

[37] Guangzhao He, Chen Geng, Shangzhe Wu, and Jiajun Wu. Category-agnostic neural object rigging. In *Proceedings of the Computer Vision and Pattern Recognition Conference*, pages 22078–22088, 2025. 1

[38] Doug L James and Christopher D Twigg. Skinning mesh animations. *ACM Transactions on Graphics (TOG)*, 24(3):399–407, 2005. 2

[39] Yuanxiang Jiang, Meng Li, Ying Fan, and Zengru Di. Characterizing dissimilarity of weighted networks. *Scientific Reports*, 11(1):5768, 2021. 2

[40] Xun Jin and Jongweon Kim. A 3d skeletonization algorithm for 3d mesh models using a partial parallel 3d thinning algorithm and 3d skeleton correcting algorithm. *Applied Sciences*, 7(2):139, 2017. 2

[41] Ladislav Kavan, P-P Sloan, and Carol O’Sullivan. Fast and efficient skinning of animated meshes. In *Computer Graphics Forum*, pages 327–336. Wiley Online Library, 2010. 2

[42] Diederik P. Kingma and Jimmy Ba. Adam: A method for stochastic optimization, 2017. 2, 5

[43] James Kirkpatrick, Razvan Pascanu, Neil Rabinowitz, Joel Veness, Guillaume Desjardins, Andrei A Rusu, Kieran Milan, John Quan, Tiago Ramalho, Agnieszka Grabska-Barwinska, et al. Overcoming catastrophic forgetting in neural networks. *Proceedings of the national academy of sciences*, 114(13):3521–3526, 2017. 6

[44] Hans Knutsson, Carl-Fredrik Westin, and Mats Andersson. Representing local structure using tensors ii. In *Scandinavian conference on image analysis*, pages 545–556. Springer, 2011. 3

[45] Binh Huy Le and Zhigang Deng. Robust and accurate skeletal rigging from mesh sequences. *ACM Transactions on Graphics (TOG)*, 33(4):1–10, 2014. 2

[46] Yann LeCun, Yoshua Bengio, and Geoffrey Hinton. Deep learning. *nature*, 521(7553):436–444, 2015. 1

[47] John P Lewis, Matt Cordner, and Nickson Fong. Pose space deformation: a unified approach to shape interpolation and skeleton-driven deformation. In *Seminal Graphics Papers: Pushing the Boundaries, Volume 2*, pages 811–818. 2023. 1, 2

[48] Peizhuo Li, Kfir Aberman, Rana Hanocka, Libin Liu, Olga Sorkine-Hornung, and Baoquan Chen. Learning skeletal articulations with neural blend shapes. *ACM Transactions on Graphics (TOG)*, 40(4):1–15, 2021. 1

[49] Yujia Li, Chenjie Gu, Thomas Dullien, Oriol Vinyals, and Pushmeet Kohli. Graph matching networks for learning the similarity of graph structured objects. In *International conference on machine learning*, pages 3835–3845. PMLR, 2019. 2

[50] Yang Li, Hikari Takehara, Takafumi Taketomi, Bo Zheng, and Matthias Nießner. 4dcomplete: Non-rigid motion estimation beyond the observable surface. In *Proceedings of the IEEE/CVF International Conference on Computer Vision*, pages 12706–12716, 2021. 5

[51] Chendi Lin, Heshan Liu, Qunshu Lin, Zachary Bright, Shitao Tang, Yihui He, Minghao Liu, Ling Zhu, and Cindy Le. Objaverse++: Curated 3d object dataset with quality annotations. *arXiv preprint arXiv:2504.07334*, 2025. 2

[52] Kevin Lin, Lijuan Wang, and Zicheng Liu. End-to-end human pose and mesh reconstruction with transformers. In *Proceedings of the IEEE/CVF conference on computer vision and pattern recognition*, pages 1954–1963, 2021. 2

[53] Isabella Liu, Hao Su, and Xiaolong Wang. Dynamic gaussians mesh: Consistent mesh reconstruction from dynamic scenes. In *The Thirteenth International Conference on Learning Representations*. 2

[54] Isabella Liu, Zhan Xu, Wang Yifan, Hao Tan, Zexiang Xu, Xiaolong Wang, Hao Su, and Zifan Shi. Riganything: Template-free autoregressive rigging for diverse 3d assets. *ACM Transactions on Graphics (TOG)*, 44(4):1–12, 2025. 1

[55] Lijuan Liu, Youyi Zheng, Di Tang, Yi Yuan, Changjie Fan, and Kun Zhou. Neuroskinning: Automatic skin binding for production characters with deep graph networks. *ACM Transactions on Graphics (ToG)*, 38(4):1–12, 2019. 1

[56] Nikita Lomov. Skeleton-geodesic distances for shape recognition: Efficient computation by continuous skeleton. In *VISIGRAPP (4: VISAPP)*, pages 307–314, 2020. [2](#)

[57] Ilya Loshchilov and Frank Hutter. Decoupled weight decay regularization. *arXiv preprint arXiv:1711.05101*, 2017. [2](#), [5](#)

[58] Jing Ma and Dongliang Zhang. Tarig: Adaptive template-aware neural rigging for humanoid characters. *Computers & Graphics*, 114:158–167, 2023. [1](#)

[59] Nadia Magnenat-Thalmann, Richard Laperrière, and Daniel Thalmann. Joint-dependent local deformations for hand animation and object grasping. In *Proceedings on Graphics interface’88*, pages 26–33, 1989. [2](#)

[60] Khaled Mamou, Titus Zaharia, and Françoise Prêteux. A skinning approach for dynamic 3d mesh compression. *Computer Animation and Virtual Worlds*, 17(3-4):337–346, 2006. [2](#)

[61] David Marr and Herbert Keith Nishihara. Representation and recognition of the spatial organization of three-dimensional shapes. *Proceedings of the Royal Society of London. Series B. Biological Sciences*, 200(1140):269–294, 1978. [1](#)

[62] Michael McCloskey and Neal J Cohen. Catastrophic interference in connectionist networks: The sequential learning problem. In *Psychology of learning and motivation*, pages 109–165. Elsevier, 1989. [6](#)

[63] Facundo Mémoli. Gromov–wasserstein distances and the metric approach to object matching. *Foundations of computational mathematics*, 11(4):417–487, 2011. [2](#)

[64] Facundo Mémoli. The gromov–wasserstein distance: A brief overview. *Axioms*, 3(3):335–341, 2014. [2](#)

[65] Anastasia Moutafidou, Vasileios Toulatzis, and Ioannis Fudos. Deep fusible skinning of animation sequences. *The Visual Computer*, 40(8):5695–5715, 2024. [2](#)

[66] Verónica Costa Orvalho, Ernesto Zacur, and Antonio Susin. Transferring the rig and animations from a character to different face models. In *Computer Graphics Forum*, pages 1997–2012. Wiley Online Library, 2008. [2](#)

[67] JunJun Pan, Xiaosong Yang, Xin Xie, Philip Willis, and Jian J Zhang. Automatic rigging for animation characters with 3d silhouette. *Computer Animation and Virtual Worlds*, 20(2-3):121–131, 2009. [2](#)

[68] Xiaoyu Pan, Jiancong Huang, Jiaming Mai, He Wang, Honglin Li, Tongkui Su, Wenjun Wang, and Xiaogang Jin. Heterskinnet: A heterogeneous network for skin weights prediction. In *Proceedings of the ACM on computer graphics and interactive techniques*. Association for Computing Machinery, 2021. [1](#)

[69] Natapon Pantuwong and Masanori Sugimoto. A fully automatic rigging algorithm for 3d character animation. In *SIGGRAPH Asia 2011 Posters*, pages 1–1. 2011. [2](#)

[70] Natapon Pantuwong and Masanori Sugimoto. A novel template-based automatic rigging algorithm for articulated character animation. *Computer Animation and Virtual Worlds*, 23(2):125–141, 2012. [2](#)

[71] Chunghyun Park, Yoonwoo Jeong, Minsu Cho, and Jaesik Park. Fast point transformer. In *Proceedings of the IEEE/CVF conference on computer vision and pattern recognition*, pages 16949–16958, 2022. [2](#)

[72] Can Qin, Handong Zhao, Lichen Wang, Huan Wang, Yulun Zhang, and Yun Fu. Slow learning and fast inference: Efficient graph similarity computation via knowledge distillation. *Advances in Neural Information Processing Systems*, 34:14110–14121, 2021. [2](#)

[73] Alec Radford, Karthik Narasimhan, Tim Salimans, Ilya Sutskever, et al. Improving language understanding by generative pre-training. 2018. [1](#), [3](#)

[74] Rishabh Ranjan, Siddharth Grover, Sourav Medya, Venkatesan Chakaravarthy, Yogish Sabharwal, and Sayan Ranu. Greed: A neural framework for learning graph distance functions. *Advances in Neural Information Processing Systems*, 35:22518–22530, 2022. [2](#)

[75] Remy Sabathier, Niloy J Mitra, and David Novotny. Animal avatars: Reconstructing animatable 3d animals from casual videos. In *European Conference on Computer Vision*, pages 270–287. Springer, 2024. [2](#)

[76] Peter H Schönenmann. A generalized solution of the orthogonal procrustes problem. *Psychometrika*, 31(1):1–10, 1966. [3](#)

[77] Yahao Shi, Yang Liu, Yanmin Wu, Xing Liu, Chen Zhao, Jie Luo, and Bin Zhou. Drive any mesh: 4d latent diffusion for mesh deformation from video. *arXiv preprint arXiv:2506.07489*, 2025. [2](#)

[78] Chaoyue Song, Jiacheng Wei, Chuan Sheng Foo, Guosheng Lin, and Fayao Liu. Reacto: Reconstructing articulated objects from a single video. In *Proceedings of the IEEE/CVF Conference on Computer Vision and Pattern Recognition*, pages 5384–5395, 2024. [2](#)

[79] Chaoyue Song, Xiu Li, Fan Yang, Zhongcong Xu, Jiacheng Wei, Fayao Liu, Jiashi Feng, Guosheng Lin, and Jianfeng Zhang. Puppeteer: Rig and animate your 3d models. *arXiv preprint arXiv:2508.10898*, 2025. [1](#), [2](#)

[80] Chaoyue Song, Jiacheng Wei, Tianyi Chen, Yiwen Chen, Chuan-Sheng Foo, Fayao Liu, and Guosheng Lin. Moda: Modeling deformable 3d objects from casual videos. *International Journal of Computer Vision*, 133(5):2825–2844, 2025. [2](#)

[81] Chaoyue Song, Jianfeng Zhang, Xiu Li, Fan Yang, Yiwen Chen, Zhongcong Xu, Jun Hao Liew, Xiaoyang Guo, Fayao Liu, Jiashi Feng, et al. Magicarticulate: Make your 3d models articulation-ready. In *Proceedings of the Computer Vision and Pattern Recognition Conference*, pages 15998–16007, 2025. [1](#), [2](#)

[82] Keqiang Sun, Dor Litvak, Yunzhi Zhang, Hongsheng Li, Jiajun Wu, and Shangzhe Wu. Ponymation: Learning articulated 3d animal motions from unlabeled online videos. In *European Conference on Computer Vision*, pages 100–119. Springer, 2024. [2](#)

[83] Mingze Sun, Junhao Chen, Junting Dong, Yurun Chen, Xinyu Jiang, Shiwei Mao, Puhua Jiang, Jingbo Wang, Bo Dai, and Ruqi Huang. Drive: Diffusion-based rigging empowers generation of versatile and expressive characters. In *Proceedings of the Computer Vision and Pattern Recognition Conference*, pages 21170–21180, 2025. [1](#)

[84] Mingze Sun, Shiwei Mao, Keyi Chen, Yurun Chen, Shunlin Lu, Jingbo Wang, Junting Dong, and Ruqi Huang. Armo: Autoregressive rigging for multi-category objects. *arXiv preprint arXiv:2503.20663*, 2025. 1

[85] Andrea Tagliasacchi, Hao Zhang, and Daniel Cohen-Or. Curve skeleton extraction from incomplete point cloud. In *ACM SIGGRAPH 2009 papers*, pages 1–9. 2009. 2

[86] Andrea Tagliasacchi, Ibraheem Alhashim, Matt Olson, and Hao Zhang. Mean curvature skeletons. In *Computer Graphics Forum*, pages 1735–1744. Wiley Online Library, 2012. 2

[87] Jeff Tan, Donglai Xiang, Shubham Tulsiani, Deva Ramanan, and Gengshan Yang. Dressrecon: Freeform 4d human reconstruction from monocular video. In *2025 International Conference on 3D Vision (3DV)*, pages 250–260. IEEE, 2025. 2

[88] Guy Tevet, Brian Gordon, Amir Hertz, Amit H Bermano, and Daniel Cohen-Or. Motionclip: Exposing human motion generation to clip space. In *European Conference on Computer Vision*, pages 358–374. Springer, 2022. 2

[89] The Models-Resource. The models-resource, 2019. 2, 7

[90] Anton Tsitsulin, Davide Mottin, Panagiotis Karras, Alexander Bronstein, and Emmanuel Müller. Netlsd: hearing the shape of a graph. In *Proceedings of the 24th ACM SIGKDD international conference on knowledge discovery & data mining*, pages 2347–2356, 2018. 2

[91] Thomas Unterthiner, Sjoerd Van Steenkiste, Karol Kurach, Raphaël Marinier, Marcin Michalski, and Sylvain Gelly. Fvd: A new metric for video generation. 2019. 2

[92] Ashish Vaswani, Noam Shazeer, Niki Parmar, Jakob Uszkoreit, Llion Jones, Aidan N Gomez, Łukasz Kaiser, and Illia Polosukhin. Attention is all you need. *Advances in neural information processing systems*, 30, 2017. 1

[93] Shen Wang, Zhengzhang Chen, Xiao Yu, Ding Li, Jingchao Ni, Lu-An Tang, Jiaping Gui, Zhichun Li, Haifeng Chen, and Philip S Yu. Heterogeneous graph matching networks. *arXiv preprint arXiv:1910.08074*, 2019. 2

[94] Shangzhe Wu, Ruining Li, Tomas Jakab, Christian Rupprecht, and Andrea Vedaldi. Magicpony: Learning articulated 3d animals in the wild. In *Proceedings of the IEEE/CVF Conference on Computer Vision and Pattern Recognition*, pages 8792–8802, 2023. 2

[95] Xiaoyang Wu, Li Jiang, Peng-Shuai Wang, Zhijian Liu, Xihui Liu, Yu Qiao, Wanli Ouyang, Tong He, and Hengshuang Zhao. Point transformer v3: Simpler faster stronger. In *Proceedings of the IEEE/CVF conference on computer vision and pattern recognition*, pages 4840–4851, 2024. 2

[96] Zijie Wu, Chaohui Yu, Fan Wang, and Xiang Bai. Animateanymesh: A feed-forward 4d foundation model for text-driven universal mesh animation. *arXiv preprint arXiv:2506.09982*, 2025. 2

[97] Hongteng Xu, Dixin Luo, Hongyuan Zha, and Lawrence Carin Duke. Gromov-wasserstein learning for graph matching and node embedding. In *International conference on machine learning*, pages 6932–6941. PMLR, 2019. 2

[98] Yao Xu, Bo Wang, Wenyu Liu, and Xiang Bai. Skeleton graph matching based on critical points using path similarity. In *Asian Conference on Computer Vision*, pages 456–465. Springer, 2009. 2

[99] Yunwen Xu, Srinivasa M Salapaka, and Carolyn L Beck. A distance metric between directed weighted graphs. In *52nd IEEE Conference on Decision and Control*, pages 6359–6364. IEEE, 2013. 2

[100] Zhan Xu, Yang Zhou, Evangelos Kalogerakis, and Karan Singh. Predicting animation skeletons for 3d articulated models via volumetric nets. In *2019 international conference on 3D vision (3DV)*, pages 298–307. IEEE, 2019. 2, 7

[101] Zhan Xu, Yang Zhou, Evangelos Kalogerakis, Chris Landreth, and Karan Singh. Rignet: neural rigging for articulated characters. *ACM Transactions on Graphics (TOG)*, 39(4):58:1–, 2020. 1, 2

[102] Zhan Xu, Yang Zhou, Li Yi, and Evangelos Kalogerakis. Morig: Motion-aware rigging of character meshes from point clouds. In *SIGGRAPH Asia 2022 conference papers*, pages 1–9, 2022. 2

[103] Yajie Yan, Kyle Sykes, Erin Chambers, David Letscher, and Tao Ju. Erosion thickness on medial axes of 3d shapes. *ACM Transactions on Graphics (TOG)*, 35(4):1–12, 2016. 2

[104] Yajie Yan, David Letscher, and Tao Ju. Voxel cores: Efficient, robust, and provably good approximation of 3d medial axes. *ACM Transactions on Graphics (TOG)*, 37(4):1–13, 2018. 2

[105] Gengshan Yang, Deqing Sun, Varun Jampani, Daniel Vlasic, Forrester Cole, Huiwen Chang, Deva Ramanan, William T Freeman, and Ce Liu. Lasr: Learning articulated shape reconstruction from a monocular video. In *Proceedings of the IEEE/CVF Conference on Computer Vision and Pattern Recognition*, pages 15980–15989, 2021. 2

[106] Gengshan Yang, Minh Vo, Natalia Neverova, Deva Ramanan, Andrea Vedaldi, and Hanbyul Joo. Banmo: Building animatable 3d neural models from many casual videos. In *Proceedings of the IEEE/CVF Conference on Computer Vision and Pattern Recognition*, pages 2863–2873, 2022. 2

[107] Yuxin Yao, Zhi Deng, and Junhui Hou. Riggs: Rigging of 3d gaussians for modeling articulated objects in videos. In *Proceedings of the Computer Vision and Pattern Recognition Conference*, pages 5592–5601, 2025. 2

[108] Jungjae Yoo and Hakgu Kim. A comprehensive pipeline for large-scale 3d humanoid rigging dataset creation. *TECHART: Journal of Arts and Imaging Science*, 12(3):54–60, 2025. 1

[109] Xumin Yu, Lulu Tang, Yongming Rao, Tiejun Huang, Jie Zhou, and Jiwen Lu. Point-bert: Pre-training 3d point cloud transformers with masked point modeling. In *Proceedings of the IEEE/CVF conference on computer vision and pattern recognition*, pages 19313–19322, 2022. 2

[110] Yu-Jie Yuan, Leif Kobbelt, Jiwen Liu, Yuan Zhang, Pengfei Wan, Yu-Kun Lai, and Lin Gao. 4dynamic: Text-to-4d generation with hybrid priors. *CoRR*, 2024. 2

[111] Chong Zeng, Yue Dong, Pieter Peers, Hongzhi Wu, and Xin Tong. Renderformer: Transformer-based neural rendering

of triangle meshes with global illumination. In *Proceedings of the Special Interest Group on Computer Graphics and Interactive Techniques Conference Conference Papers*, pages 1–11, 2025. [2](#)

[112] Cheng Zhang, Haocheng Wan, Xinyi Shen, and Zizhao Wu. Patchformer: An efficient point transformer with patch attention. In *Proceedings of the IEEE/CVF conference on computer vision and pattern recognition*, pages 11799–11808, 2022. [2](#)

[113] Hao Zhang, Di Chang, Fang Li, Mohammad Soleymani, and Narendra Ahuja. Magicpose4d: Crafting articulated models with appearance and motion control. *arXiv preprint arXiv:2405.14017*, 2024. [2](#)

[114] Jia-Peng Zhang, Cheng-Feng Pu, Meng-Hao Guo, Yan-Pei Cao, and Shi-Min Hu. One model to rig them all: Diverse skeleton rigging with unirig. *ACM Transactions on Graphics (TOG)*, 44(4):1–18, 2025. [1, 2, 4, 6](#)

[115] Susan Zhang, Stephen Roller, Naman Goyal, Mikel Artetxe, Moya Chen, Shuohui Chen, Christopher Dewan, Mona Diab, Xian Li, Xi Victoria Lin, et al. Opt: Open pre-trained transformer language models. *arXiv preprint arXiv:2205.01068*, 2022. [2](#)

[116] Yibo Zhang, Li Zhang, Rui Ma, and Nan Cao. Texverse: A universe of 3d objects with high-resolution textures. *arXiv preprint arXiv:2508.10868*, 2025. [2](#)

[117] Zhen Zhang, Jiajun Bu, Martin Ester, Zhao Li, Cheng-wei Yao, Zhi Yu, and Can Wang. H2mn: Graph similarity learning with hierarchical hypergraph matching networks. In *Proceedings of the 27th ACM SIGKDD conference on knowledge discovery & data mining*, pages 2274–2284, 2021. [2](#)

[118] Hengshuang Zhao, Li Jiang, Jiaya Jia, Philip HS Torr, and Vladlen Koltun. Point transformer. In *Proceedings of the IEEE/CVF international conference on computer vision*, pages 16259–16268, 2021. [2](#)

[119] Ce Zheng, Matias Mendieta, Pu Wang, Aidong Lu, and Chen Chen. A lightweight graph transformer network for human mesh reconstruction from 2d human pose. In *Proceedings of the 30th ACM international conference on multimedia*, pages 5496–5507, 2022. [2](#)

[120] Shanshan Zhong, Jiawei Peng, Zehan Zheng, Zhongzhan Huang, Wufei Ma, Guofeng Zhang, Qihao Liu, Alan Yuille, and Jieneng Chen. 4d-animal: Freely reconstructing animatable 3d animals from videos. *arXiv preprint arXiv:2507.10437*, 2025. [2](#)

[121] Wei Zhuo and Guang Tan. Efficient graph similarity computation with alignment regularization. *Advances in Neural Information Processing Systems*, 35:30181–30193, 2022. [2](#)

SPRig: Self-Supervised Pose-Invariant Rigging from Mesh Sequences

Supplementary Material

7. Skeleton Loss Details

7.1. Token-space loss

Recall that the token-space objective in the main paper (Eq. 2) is $\mathcal{L}_{\text{token}} = \lambda_{\text{anchor}} \mathcal{L}_{\text{anchor}} + \lambda_{\text{sym}} \mathcal{L}_{\text{sym}}$. We detail $\mathcal{L}_{\text{anchor}}$ and \mathcal{L}_{sym} here.

Let \mathcal{I} be the valid token positions in the anchor sequence. Tokens are grouped into (t_x, t_y, t_z, t_p) ; we index positions inside each quadruple 0-based, so the *parent slot* is $i \bmod 4 = 3$. Denote by $t_{(0,i)}$ the anchor token at position i and by $\mathbf{l}_{(0,i)}$ the model’s predictive distribution (logits) at that position under teacher forcing on \mathbf{F}_0 . We apply a per-position weight

$$w_i = \begin{cases} \alpha, & i \bmod 4 = 3 \text{ (parent slot),} \\ 1, & \text{otherwise,} \end{cases} \quad \alpha > 1.$$

The anchor loss is the weighted token-level cross entropy:

$$\mathcal{L}_{\text{anchor}} = \frac{\sum_{i \in \mathcal{I}} w_i \text{CE}(\mathbf{l}_{(0,i)}, t_{(0,i)})}{\sum_{i \in \mathcal{I}} w_i}. \quad (8)$$

For each non-anchor frame $k \geq 1$, we condition on \mathbf{F}_k but keep the target tokens fixed to the anchor labels; let $\mathbf{l}_{(k \leftarrow 0,i)}$ be the model’s predictive distribution at position i under teacher forcing with the anchor prefix. Using the same weights w_i ,

$$\mathcal{L}_{\text{sym}} = \frac{1}{|\mathcal{K}|} \sum_{k \in \mathcal{K}} \frac{\sum_{i \in \mathcal{I}} w_i \text{CE}(\mathbf{l}_{(k \leftarrow 0,i)}, t_{(0,i)})}{\sum_{i \in \mathcal{I}} w_i}, \quad (9)$$

where $\mathcal{K} \subseteq \{1, \dots, K-1\}$ can be uniformly subsampled for efficiency. Together with Eq. 2 in the main paper, these terms define the full token-space loss $\mathcal{L}_{\text{token}}$.

7.2. Geometry-space loss

We regularize the *inference-time* predictions (no teacher forcing). From $(\hat{\mathbf{X}}_0, \hat{\mathbf{p}}_0)$ and $(\hat{\mathbf{X}}_k, \hat{\mathbf{p}}_k)$, define the edge set

$$E_k = \{(i, j) \mid \hat{\mathbf{p}}_k[j] = i, i \neq j\},$$

the edge vectors

$$\mathcal{V}_k = \{\mathbf{v}_{ij} = \mathbf{x}_j - \mathbf{x}_i \mid (i, j) \in E_k\},$$

and the edge midpoints

$$\mathcal{M}_k = \{\mathbf{m}_{ij} = \frac{\mathbf{x}_i + \mathbf{x}_j}{2} \mid (i, j) \in E_k\}.$$

The anchor \mathcal{S}_0 and the prediction $\hat{\mathcal{S}}_k$ can be in very different poses; comparing raw joint coordinates would confound articulated motion with global rotation/translation.

We therefore estimate a rigid transform $(\mathbf{R}_k, \mathbf{t}_k)$ so the large-scale bone arrangement is aligned before measuring similarity. We obtain \mathbf{R}_k by aligning the principal axes of the structure tensors \mathbf{S}_0 and \mathbf{S}_k (Eq. 10), which only depend on edge vectors and thus are robust to joint relabeling; the weights $\omega_{ij} \propto \|\mathbf{v}_{ij}\|$ emphasize stable long bones. Translation is set by matching the means of edge midpoints (Eq. 12).

We estimate the rigid transform $(\mathbf{R}_k, \mathbf{t}_k)$ by aligning *structure tensors*

$$\mathbf{S}_k = \sum_{(i,j) \in E_k} \omega_{ij} \mathbf{v}_{ij} \mathbf{v}_{ij}^\top, \quad (10)$$

where

$$\omega_{ij} \propto \|\mathbf{v}_{ij}\|, \quad (11)$$

and setting

$$\mathbf{t}_k = \mu(\mathcal{M}_k) - \mathbf{R}_k \mu(\mathcal{M}_0), \quad (12)$$

where $\mu(\mathcal{A})$ denotes the arithmetic mean, or the centroid, of a point set \mathcal{A} .

Let $\tilde{E}_k \subseteq E_k$ be the top- ρ edges by length (unit-normalized for comparisons, $\rho \in (0, 1]$). We then use three permutation-agnostic terms comparing *directions*, *lengths*, and *endpoints*.

Directional term.

$$\begin{aligned} \mathcal{L}_{\text{dir}} = & \frac{1}{2} \left[1 - \text{mean}_{(i,j) \in \tilde{E}_0} \max_{(p,q) \in \tilde{E}_k} \left\langle \frac{\mathbf{R}_k \mathbf{v}_{ij}}{\|\mathbf{v}_{ij}\|_2}, \frac{\mathbf{v}_{pq}}{\|\mathbf{v}_{pq}\|_2} \right\rangle \right. \\ & \left. + 1 - \text{mean}_{(p,q) \in \tilde{E}_k} \max_{(i,j) \in \tilde{E}_0} \left\langle \frac{\mathbf{R}_k \mathbf{v}_{ij}}{\|\mathbf{v}_{ij}\|_2}, \frac{\mathbf{v}_{pq}}{\|\mathbf{v}_{pq}\|_2} \right\rangle \right]. \end{aligned} \quad (13)$$

Length term. Let $\{\ell^{(i)}\}$ be the sorted edge lengths after alignment. Define

$$\mathcal{L}_{\text{len}} = \frac{1}{m} \sum_{i=1}^m (\ell_k^{(i)} - \ell_0^{(i)})^2, \quad (14)$$

and

$$m = \min\{|E_0|, |E_k|\}. \quad (15)$$

Endpoint (Chamfer) term. Let \mathcal{P}_k concatenate all edge endpoints of frame k . Then

$$\begin{aligned} \mathcal{L}_{\text{ch}} = & \frac{1}{|\mathcal{P}_0|} \sum_{\mathbf{p} \in \mathcal{P}_0} \min_{\mathbf{q} \in \mathcal{P}_k} \|\mathbf{R}_k \mathbf{p} + \mathbf{t}_k - \mathbf{q}\|_2^2 \\ & + \frac{1}{|\mathcal{P}_k|} \sum_{\mathbf{q} \in \mathcal{P}_k} \min_{\mathbf{p} \in \mathcal{P}_0} \|\mathbf{R}_k \mathbf{p} + \mathbf{t}_k - \mathbf{q}\|_2^2. \end{aligned} \quad (16)$$

Finally, the geometry-space loss used in Eq. 3 of the main paper is obtained by averaging these aligned distances over non-anchor frames and taking a weighted sum of the three terms:

$$\mathcal{L}_{\text{geom}} = \frac{1}{K-1} \sum_{k=1}^{K-1} \left(\lambda_{\text{dir}} \mathcal{L}_{\text{dir}} + \lambda_{\text{len}} \mathcal{L}_{\text{len}} + \lambda_{\text{ch}} \mathcal{L}_{\text{ch}} \right).$$

8. Skinning Loss Details

8.1. Top- K_s masking and masked operators

To suppress noise in the teacher distribution, we build a Top- K_s mask $\mathbf{m} \in [0, 1]^{N \times J}$ from the point teacher \mathbf{W}^T . For each point i , we keep the Top- K_s joints (over valid joints) with mask value 1, assign a smaller value $\gamma \in [0, 1)$ to the remaining valid joints, and set mask entries on invalid joints ($\mathbf{V}_j=0$) to 0:

$$\mathbf{m}_{i,j} = \begin{cases} 1, & j \in \text{Top-}K_s(\mathbf{W}_{i,:}^T) \text{ and } \mathbf{V}_j=1, \\ \gamma, & \mathbf{V}_j=1 \text{ and } j \notin \text{Top-}K_s(\mathbf{W}_{i,:}^T), \\ 0, & \mathbf{V}_j=0. \end{cases}$$

We use two masked operators throughout (with $\varepsilon > 0$). The first renormalizes a distribution on the masked support:

$$\mathcal{R}(\mathbf{Z}; \mathbf{m}) = \frac{\mathbf{Z} \odot \mathbb{1}[\mathbf{m} > 0]}{\sum_j \mathbf{Z}_{:,j} \mathbb{1}[\mathbf{m}_{:,j} > 0] + \varepsilon}, \quad (17)$$

where \odot denotes the element-wise Hadamard product and $\mathbb{1}[\cdot]$ is an element-wise indicator.

The second is a masked averaging operator used to aggregate per-point, per-joint quantities:

$$\langle f, \mathbf{m} \rangle = \frac{1}{\sum_{i,j} \mathbf{m}_{i,j} / N} \sum_{i,j} f_{i,j} \mathbf{m}_{i,j}. \quad (18)$$

This operator averages $f_{i,j}$ over active entries weighted by $\mathbf{m}_{i,j}$ and normalized by the effective number of active entries.

8.2. Loss components for articulation-invariant consistency

We detail the components of the total loss $\mathcal{L}_{\text{total}} = \lambda_{\text{cons}} \mathcal{L}_{\text{cons}} + \lambda_{\text{reg}} \mathcal{L}_{\text{reg}}$ from Eq. 7 in the main paper.

Let $\tilde{\mathbf{Y}} = \mathcal{R}(\mathbf{W}^T; \mathbf{m})$ be the masked-and-renormalized teacher distribution, and $\tilde{\mathbf{W}}^{(k)} = \mathcal{R}(\hat{\mathbf{W}}_k; \mathbf{m})$ the corresponding normalized prediction at frame k .

Consistency distillation. We match non-anchor frames to the teacher with symmetric KL and masked L_1 :

$$\mathcal{L}_{\text{sym}} = \frac{1}{K} \sum_{k=1}^K \left\langle \text{KL}(\tilde{\mathbf{Y}} \parallel \tilde{\mathbf{W}}^{(k)}) + \text{KL}(\tilde{\mathbf{W}}^{(k)} \parallel \tilde{\mathbf{Y}}), \mathbf{m} \right\rangle, \quad (19)$$

$$\mathcal{L}_1 = \frac{1}{K} \sum_{k=1}^K \left\langle |\tilde{\mathbf{W}}^{(k)} - \tilde{\mathbf{Y}}|, \mathbf{m} \right\rangle. \quad (20)$$

We also penalize anchor-frame deviation to avoid teacher drift:

$$\mathcal{L}_{\text{anchor}} = \left\langle |\tilde{\mathbf{W}}^{(0)} - \tilde{\mathbf{Y}}|, \mathbf{m} \right\rangle. \quad (21)$$

The consistency (distillation) objective aggregates these terms:

$$\mathcal{L}_{\text{cons}} = \lambda_{\text{sym}} \mathcal{L}_{\text{sym}} + \lambda_1 \mathcal{L}_1 + \lambda_{\text{anchor}} \mathcal{L}_{\text{anchor}}. \quad (22)$$

Structural and geometric regularization. We impose generic priors that are independent of the teacher: sharp, sparse assignments and proximity to nearby bones. We discourage diffuse predictions via a masked entropy term:

$$\mathcal{L}_{\text{ent}} = \sum_{k=0}^K \left(-\langle \tilde{\mathbf{W}}^{(k)} \odot \log \tilde{\mathbf{W}}^{(k)}, \mathbf{m} \rangle \right). \quad (23)$$

For the geometric prior, let $\mathbf{a}_j = \mathbf{X}[j]$ and $\mathbf{b}_j = \mathbf{X}[\mathbf{p}_j]$ be the endpoints of bone j . For frame k and point i , let $d_{i,j}^{(k)}$ be the distance from $\mathbf{e}_i^{(k)}$ to segment $\overline{\mathbf{a}_j \mathbf{b}_j}$. Define a per-frame exponential proximity prior,

$$\Pi_{i,j}^{(k)} \propto \exp(-\beta d_{i,j}^{(k)}), \quad (24)$$

and time-average it over a short window $\mathcal{K}_{\text{avg}} \subseteq \{0, \dots, K\}$ to stabilize:

$$\Pi_{\text{avg}} = \frac{1}{|\mathcal{K}_{\text{avg}}|} \sum_{k \in \mathcal{K}_{\text{avg}}} \Pi^{(k)}. \quad (25)$$

We then align predictions to the averaged prior via KL:

$$\mathcal{L}_{\text{prior}} = \sum_{k=0}^K \left\langle \text{KL}(\mathcal{R}(\Pi_{\text{avg}}; \mathbf{m}) \parallel \tilde{\mathbf{W}}^{(k)}), \mathbf{m} \right\rangle. \quad (26)$$

The regularization objective is

$$\mathcal{L}_{\text{reg}} = \lambda_{\text{ent}} \mathcal{L}_{\text{ent}} + \lambda_{\text{prior}} \mathcal{L}_{\text{prior}}. \quad (27)$$

Combining Eqs. 22 and 27 with Eq. 7 in the main paper yields the full articulation-invariant skinning loss used in our experiments.

9. Skeleton Implementation Details

We fine-tune from the pretrained SkeletonGPT (Puppeteer) weights, which use an OPT-based [115] decoder, while keeping the trimesh [25] point cloud encoder \mathcal{E} frozen. Training is performed on a single NVIDIA A100 GPU via Google Colab using AdamW [42, 57] with a learning rate of 3×10^{-6} and a batch size of 20. Training for 50 epochs takes roughly 20 hours. During training, $\mathcal{L}_{\text{anchor}}$ is applied to frame 0, and \mathcal{L}_{sym} and $\mathcal{L}_{\text{geom}}$ are applied to frames 1 and 2. Besides, topology weight $\alpha = 3.0$, symbolic weight $\lambda_{\text{sym}} = 1.0$, and geometric weight $\lambda_{\text{geom}} = 0.5$.

10. Skeleton Consistency Evaluation Metrics

Notation. For a given clip, let the predicted skeleton at frame k be

$$\hat{S}_k = (\hat{\mathbf{X}}_k, \hat{\mathbf{p}}_k),$$

$$\hat{\mathbf{X}}_k = [\hat{\mathbf{x}}_1^{(k)}, \dots, \hat{\mathbf{x}}_J^{(k)}]^\top \in \mathbb{R}^{J \times 3},$$

where J is the number of joints and $\hat{\mathbf{p}}_k \in \{0, \dots, J\}^J$ are parent indices. We treat $k=0$ as the anchor frame and denote by

$$\tilde{\mathbf{X}}_k = \text{Procrustes}(\hat{\mathbf{X}}_k, \hat{\mathbf{X}}_0)$$

the joint coordinates of frame k after Procrustes alignment [76] onto the anchor. By convention $\tilde{\mathbf{X}}_0 = \hat{\mathbf{X}}_0$.

Let E_0 be an undirected edge set on the anchor joints, in practice the Euclidean minimum spanning tree on $\hat{\mathbf{X}}_0$. For each edge $e=(u, v) \in E_0$, we define its length at frame k as

$$\ell_k(e) = \|\tilde{\mathbf{x}}_u^{(k)} - \tilde{\mathbf{x}}_v^{(k)}\|_2,$$

and collect the sorted edge-length vectors

$$L_k = \text{sort}(\{\ell_k(e)\}_{e \in E_0}) \in \mathbb{R}^{|E_0|}.$$

For pairwise joint distances, let

$$D_k = (d_k(i, j))_{1 \leq i < j \leq J} \in \mathbb{R}^M,$$

$$d_k(i, j) = \|\tilde{\mathbf{x}}_i^{(k)} - \tilde{\mathbf{x}}_j^{(k)}\|_2,$$

where $M = \binom{J}{2}$. We write $\text{median}(\cdot)$ for the median of a set of scalars and use a small numerical floor $\varepsilon > 0$ when needed.

10.1. Pairwise Joint Distance Deviation (PJDD)

PJDD measures how much the distribution of joint-to-joint distances drifts away from the anchor frame after rigid alignment. For each aligned non-anchor frame, we compute all pairwise joint distances, sort them into a list, and compare this list with the corresponding list at the anchor by taking absolute differences, normalizing by a typical scale from the anchor distances, and averaging over all pairs. A lower value means less geometric jitter over time.

For a non-anchor frame $k \geq 1$, PJDD is

$$\text{PJDD}_k = \frac{1}{M} \sum_{m=1}^M \frac{|D_k^{(m)} - D_0^{(m)}|}{\max(\text{median}(D_0), \varepsilon)}. \quad (28)$$

For each clip we average over non-anchor frames, then report the mean PJDD across clips.

10.2. Bone Length Relative Deviation (BLRD)

BLRD measures how much individual bone lengths change over time with respect to a fixed anchor topology. We use a fixed set of undirected edges on the anchor skeleton as the bone graph. For each aligned non-anchor frame, we measure the length of every edge in this set, sort these lengths, and compare them with the sorted anchor lengths using normalized absolute differences averaged over edges. Lower BLRD means bones keep more consistent length and the structure flickers less.

For a non-anchor frame $k \geq 1$, BLD is

$$\text{BLRD}_k = \frac{1}{|E_0|} \sum_{i=1}^{|E_0|} \frac{|L_k^{(i)} - L_0^{(i)}|}{\max(\text{median}(L_0), \varepsilon)}. \quad (29)$$

We average BLD over non-anchor frames per clip and then across clips.

10.3. Graph Spectral Discrepancy (GSD)

GSD summarizes how much the global skeletal graph structure changes over time. Using the fixed edge set, we build a weighted graph on the aligned joints for each frame, where each edge weight is proportional to the corresponding bone length and normalized by a characteristic anchor scale. From this graph we form the normalized Laplacian and compute its smallest eigenvalues. For each non-anchor frame, we compare its eigenvalue list with that of the anchor by taking the average absolute difference across the first few entries. A lower GSD means the overall skeletal graph, in terms of connectivity and relative bone strengths, stays closer to the anchor.

Given E_0 and $\tilde{\mathbf{X}}_k$, we build a symmetric weight matrix $W^{(k)} \in \mathbb{R}^{J \times J}$ by

$$W_{uv}^{(k)} = \begin{cases} \frac{\|\tilde{\mathbf{x}}_u^{(k)} - \tilde{\mathbf{x}}_v^{(k)}\|_2}{\max(\text{median}(L_0), \varepsilon)}, & (u, v) \in E_0, \\ 0, & \text{otherwise.} \end{cases}$$

Let $\mathbf{d}^{(k)}$ be the degree vector, $d_u^{(k)} = \sum_v W_{uv}^{(k)}$, and $D^{(k)} = \text{diag}(\mathbf{d}^{(k)})$. The normalized graph Laplacian at frame k is

$$\mathcal{L}^{(k)} = I - (D^{(k)})^{-\frac{1}{2}} W^{(k)} (D^{(k)})^{-\frac{1}{2}}.$$

Let $\lambda_1^{(k)} \leq \dots \leq \lambda_N^{(k)}$ be the first N eigenvalues of $\mathcal{L}^{(k)}$; we use $N=8$ in all experiments. GSD is

$$\text{GSD}_k = \frac{1}{N} \sum_{r=1}^N |\lambda_r^{(k)} - \lambda_r^{(0)}|. \quad (30)$$

We average GSD_k over non-anchor frames per clip and report the dataset mean.

10.4. Joint Angle Discrepancy (JAD)

JAD measures how much bone orientations rotate relative to the anchor. For each edge in the fixed edge set, we form a unit direction vector at the anchor and a unit direction vector at each aligned non-anchor frame. We compute the angle between these directions, normalize it to the range from zero to one, and average over all edges. A smaller value means that bones keep more similar directions across time and the articulated structure is more stable.

For each edge $e=(u, v) \in E_0$, define the unit bone direction at the anchor and at frame k as

$$\mathbf{a}_{uv} = \frac{\hat{\mathbf{x}}_v^{(0)} - \hat{\mathbf{x}}_u^{(0)}}{\|\hat{\mathbf{x}}_v^{(0)} - \hat{\mathbf{x}}_u^{(0)}\|_2},$$

$$\mathbf{b}_{uv}^{(k)} = \frac{\tilde{\mathbf{x}}_v^{(k)} - \tilde{\mathbf{x}}_u^{(k)}}{\|\tilde{\mathbf{x}}_v^{(k)} - \tilde{\mathbf{x}}_u^{(k)}\|_2}.$$

The per-edge normalized angle difference is

$$\delta_{uv}^{(k)} = \frac{1}{\pi} \arccos (\langle \mathbf{a}_{uv}, \mathbf{b}_{uv}^{(k)} \rangle) \in [0, 1].$$

JAD for frame k is

$$\text{JAD}_k = \frac{1}{|E_0|} \sum_{(u,v) \in E_0} \delta_{uv}^{(k)}. \quad (31)$$

We report the mean JAD over non-anchor frames and clips as an additional diagnostic.

10.5. MPJPE@Anchor

MPJPE@Anchor evaluates absolute accuracy at the anchor frame. We compare the predicted anchor joints with the ground-truth anchor joints in the same canonical coordinate system. For each joint we compute the Euclidean distance between the prediction and the ground truth, then average these distances over all joints. This gives a single static error that complements the temporal stability metrics.

Let $\mathbf{X}_0^{\text{GT}} = [\mathbf{x}_{0,1}^{\text{GT}}, \dots, \mathbf{x}_{0,J}^{\text{GT}}]^\top$ be the ground-truth anchor joints. The MPJPE at the anchor frame is

$$\text{MPJPE@Anchor} = \frac{1}{J} \sum_{j=1}^J \|\hat{\mathbf{x}}_j^{(0)} - \mathbf{x}_{0,j}^{\text{GT}}\|_2. \quad (32)$$

10.6. Static Chamfer Distance Metrics

For static generation quality, we evaluate on the Articulation-XLv2 benchmark using standard Chamfer distance variants. CD-J2J compares predicted joints with ground-truth joints. For each predicted joint we find the closest ground-truth joint and average these distances, then swap the roles and average again, and finally take the mean of the two directions. CD-J2B compares predicted joints

with sampled points along ground-truth bones in the same symmetric way. CD-B2B compares sampled points along predicted bones with sampled points along ground-truth bones. In all three cases, lower values indicate that the predicted skeletons are better aligned with the ground-truth rigs in space.

11. Additional Skeleton Generation Baseline Analysis: UniRig

To provide a more comprehensive comparison, we evaluated an additional state-of-the-art autoregressive baseline, *UniRig* [114], on our full temporal stability protocol. The results are presented in Tab. 6, which extends the main paper’s Tab. 1 (Puppeteer and SPRig) with the new UniRig data.

Table 6. Extended Temporal Stability Comparison on DeformingThings4D. We compare our *SPRig* against the *Puppeteer* baseline (from the main paper) and the *UniRig* baseline. Note *UniRig*’s paradoxical results: excellent BLRD/GSD scores but catastrophic MPJPE@Anchor and poor PJDD.

Model	PJDD (↓)	BLRD (↓)	GSD (↓)	JAD (diag.)	MPJPE@Anchor (diag.)
Puppeteer	17.46	34.37	0.062	0.343	0.592
UniRig	2.76	13.25	0.022	0.28	1.327
SPRig	0.68	17.74	0.056	0.380	0.731

11.1. Analysis of Results

The Apparent Paradox. At first glance, the *UniRig* results appear contradictory. It achieves the best scores on BLRD, GSD, and the diagnostic JAD metric, suggesting high stability. However, it performs poorly on PJDD (over 4× worse than our *SPRig*) and suffers from a catastrophically high MPJPE@Anchor (over 2.2× worse than the Puppeteer baseline).

Key Insight: Catastrophic Anchor Failure. The root cause of this paradox is revealed by the MPJPE@Anchor score. *UniRig*’s anchor-frame error of 1.327 is prohibitively high, indicating that it fails to generate a high-quality static skeleton even for the initial anchor frame $\hat{\mathcal{S}}_0$.

This initial failure fundamentally compromises all stability metrics that rely on this anchor’s topology. Our BLRD and GSD metrics are by design sparse; they are computed based on the Euclidean Minimum Spanning Tree (MST) of the anchor, E_0 , which contains only $J - 1$ edges. If the anchor $\hat{\mathcal{S}}_0$ is itself a poor-quality prediction, the resulting E_0 is not a meaningful representation of the true bone topology, and the BLRD/GSD scores become unreliable. This is precisely why we explicitly separate static quality (MPJPE@Anchor, measured against ground-truth anchors) from temporal stability (BLRD/PJDD/GSD/JAD, measured relative to the predicted anchor), and why dense metrics like

PJDD are essential to diagnose degenerate but internally consistent predictions.

Sparse vs. Dense Metrics: Why PJDD is Crucial. UniRig appears to enter a “frozen rig” regime: most joints move very little over time, leading to a low JAD, but a small number of severely misplaced joints exhibit inconsistent behaviour across frames. Because BLRD/GSD only see these outliers through a handful of MST edges, their contribution is heavily diluted, whereas the dense PJDD metric aggregates all $J - 1$ distances associated with each outlier joint, and therefore reveals the underlying geometric jitter.

Conclusion. In summary, UniRig’s low BLRD/GSD and JAD scores mainly reflect that its predicted skeleton sequences are internally consistent with a severely mispredicted anchor, rather than truly stable and accurate rigs. The dense PJDD metric, together with the static MPJPE@Anchor, reveals that UniRig actually suffers from both poor anchor quality and significant geometric jitter around a few outlier joints. In contrast, SPRig achieves substantially lower MPJPE@Anchor and PJDD while maintaining competitive BLRD and GSD, indicating that it provides both high static accuracy and genuine temporal stability under our evaluation protocol. This analysis therefore validates the necessity of our full metric suite, proving that reliance on any single metric can be actively misleading and fails to capture complex failure modes.

12. Skinning Implementation Details

We conduct experiments on DT4D using our predefined training and test splits. A pretrained backbone is fine-tuned (see Sec. 4.1), with the publicly available Puppeteer checkpoint serving as the baseline S_ϕ (pretrained and frozen). Optimization is performed using the AdamW optimizer [42, 57] with a learning rate of 1e-5, a batch size of 12, automatic mixed precision (AMP), and one gradient accumulation step. Our main model (v3) is trained for 50 epochs, requiring about 1 h on a single NVIDIA A100 GPU. For the ablation study (v2), all models are trained for 12 epochs. For the loss terms (Eq. 7), we set $\lambda_{\text{sym}}=1.0$, $\lambda_1=1.0$, $\lambda_{\text{anchor}}=0.25$, $\lambda_{\text{ent}}=0.02$, and $\lambda_{\text{prior}}=0.1$. For the Top- K_s mask, we use $K_s=4$ and $\gamma=0$. The geometric prior (Eq. (24)) uses $\beta=15.0$ with a $T=5$ epoch linear warmup for λ_{prior} . We use 4 dataloader workers with a prefetch factor of 4 and filter out samples containing fewer than 10 valid joints.

13. Skinning Consistency Evaluation Metrics

Notation. For a given clip, let the animated mesh at frame k be

$$\mathbf{M}_k = (\mathbf{V}^{(k)}, \mathbf{F}),$$

$$\mathbf{V}^{(k)} = [\mathbf{v}_1^{(k)}, \dots, \mathbf{v}_{N_v}^{(k)}]^\top \in \mathbb{R}^{N_v \times 3},$$

where $\mathbf{F} \in \{1, \dots, N_v\}^{N_f \times 3}$ is a fixed triangle index set (consistent topology across frames). We treat $k=0$ as the anchor frame.

We sample N surface points on the anchor mesh by area-weighted triangle sampling and barycentric interpolation. For each sampled point i , let $f_i \in \{1, \dots, N_f\}$ denote the sampled face and $\lambda_i = (\lambda_{i,1}, \lambda_{i,2}, \lambda_{i,3}) \in \Delta^2$ the barycentric coordinates. Denoting the vertices of face f_i at frame k by

$$(\mathbf{v}_{f_i,1}^{(k)}, \mathbf{v}_{f_i,2}^{(k)}, \mathbf{v}_{f_i,3}^{(k)}),$$

the corresponding point position is

$$\mathbf{e}_i^{(k)} = \sum_{r=1}^3 \lambda_{i,r} \mathbf{v}_{f_i,r}^{(k)} \in \mathbb{R}^3.$$

We similarly define a unit-length normal $\mathbf{n}_i^{(k)} \in \mathbb{R}^3$ from the triangle normal. Each frame hence yields a query pair

$$\mathbf{u}_i^{(k)} = [\mathbf{e}_i^{(k)} \ \mathbf{n}_i^{(k)}] \in \mathbb{R}^6,$$

$$\mathbf{U}_k = [\mathbf{u}_1^{(k)}, \dots, \mathbf{u}_N^{(k)}]^\top \in \mathbb{R}^{N \times 6}.$$

Let $\mathbf{X} \in \mathbb{R}^{J \times 3}$ be the anchor-normalized joint positions, and $\mathbf{p} \in \{0, \dots, J\}^J$ the parent indices with a valid joint mask $\mathbf{V} \in \{0, 1\}^J$. The skinning predictor H_ϕ maps $(\mathbf{U}_k; \mathbf{X}, \mathbf{p}, \mathbf{V}, \mathbf{D})$ to per-point joint distributions:

$$\hat{\mathbf{W}}_k = H_\phi(\mathbf{U}_k; \mathbf{X}, \mathbf{p}, \mathbf{V}, \mathbf{D}),$$

$$\hat{\mathbf{W}}_k \in \mathbb{R}^{N \times J},$$

$$\hat{\mathbf{W}}_k[i, :] \in \Delta^{J-1}.$$

13.1. Barycentric correspondences and anchor teacher

On the anchor frame $k=0$, we assume access to a high-quality vertex-level teacher

$$\mathbf{W}_{\text{vtx}}^T \in \mathbb{R}^{N_v \times J_{\text{valid}}},$$

whose columns correspond to the subset of valid joints ($\mathbf{V}_j=1$). For each sampled point i , the anchor position is

$$\mathbf{e}_i^{(0)} = \sum_{r=1}^3 \lambda_{i,r} \mathbf{v}_{f_i,r}^{(0)}, \quad (33)$$

and the corresponding teacher distribution is obtained by barycentric interpolation of the three vertex teachers:

$$\mathbf{W}_{i,:}^T = \sum_{r=1}^3 \lambda_{i,r} (\mathbf{W}_{\text{vtx}}^T)_{f_i,r,:} \in \mathbb{R}^{J_{\text{valid}}}. \quad (34)$$

We pad $\mathbf{W}_{i,:}^T$ with zeros on invalid joints to obtain a point-level teacher

$$\mathbf{W}^T \in \mathbb{R}^{N \times J},$$

which is shared by all frames in the clip and acts as a pose-invariant canonical target.

In practice, we suppress noise in the teacher tails by applying a Top- K_s mask $\mathbf{m} \in [0, 1]^{N \times J}$ and the masked renormalization operator $\mathcal{R}(\cdot; \mathbf{m})$ and averaging operator $\langle \cdot, \mathbf{m} \rangle$ (see Sec. 8 for their definitions). We denote the masked and renormalized teacher and predictions by

$$\begin{aligned} \tilde{\mathbf{Y}} &= \mathcal{R}(\mathbf{W}^T; \mathbf{m}), \\ \tilde{\hat{\mathbf{W}}}^{(k)} &= \mathcal{R}(\hat{\mathbf{W}}_k; \mathbf{m}). \end{aligned}$$

13.2. Teacher-based temporal consistency metrics

We evaluate temporal consistency by comparing predictions on non-anchor frames against the shared anchor teacher, using three metrics. Let $\mathcal{K}_{\text{na}} \subseteq \{1, \dots, K\}$ denote the set of non-anchor frame indices.

$L_1(B, C \rightarrow A)$. The teacher-aligned L_1 error is the average masked L_1 distance between non-anchor predictions and the anchor teacher:

$$L_1(B, C \rightarrow A) = \frac{1}{|\mathcal{K}_{\text{na}}|} \sum_{k \in \mathcal{K}_{\text{na}}} \left\langle \left| \tilde{\hat{\mathbf{W}}}^{(k)} - \tilde{\mathbf{Y}} \right|, \mathbf{m} \right\rangle. \quad (35)$$

Lower values indicate that the predicted attachments on perturbed frames remain close to the anchor teacher.

$SymKL(B, C \leftrightarrow A)$. We measure distributional similarity via a symmetric KL divergence:

$$\begin{aligned} SymKL(B, C \leftrightarrow A) &= \\ &\frac{1}{|\mathcal{K}_{\text{na}}|} \sum_{k \in \mathcal{K}_{\text{na}}} \left\langle \text{KL}(\tilde{\mathbf{Y}} \parallel \tilde{\hat{\mathbf{W}}}^{(k)}) + \text{KL}(\tilde{\hat{\mathbf{W}}}^{(k)} \parallel \tilde{\mathbf{Y}}), \mathbf{m} \right\rangle. \end{aligned} \quad (36)$$

Lower SymKL indicates that the shapes of the attachment distributions are more consistent across frames.

Entropy. To assess prediction sharpness, we compute the masked entropy of the predictions on all frames:

$$Entropy = \frac{1}{K+1} \sum_{k=0}^K \left(- \left\langle \tilde{\hat{\mathbf{W}}}^{(k)} \odot \log \tilde{\hat{\mathbf{W}}}^{(k)}, \mathbf{m} \right\rangle \right). \quad (37)$$

Lower entropy corresponds to more confident (sparser) attachment distributions.

13.3. Per-joint weighted temporal variance (diagnostic)

In addition to the teacher-based metrics above, we use a teacher-free, per-joint variance metric as a diagnostic to identify joints whose temporal stability benefits most from fine-tuning.

For a fixed model (original or fine-tuned) and a set of frames \mathcal{K}_{var} (typically $\{0, 1, 2\}$), let $\hat{\mathbf{W}}^{(k)} \in \mathbb{R}^{N \times J}$ be the predicted weights at frame k . For each joint j and point i , define the per-point temporal mean and variance

$$\begin{aligned} \bar{w}_{i,j} &= \frac{1}{|\mathcal{K}_{\text{var}}|} \sum_{k \in \mathcal{K}_{\text{var}}} \hat{W}_{i,j}^{(k)}, \\ \text{var}_{i,j} &= \frac{1}{|\mathcal{K}_{\text{var}}|} \sum_{k \in \mathcal{K}_{\text{var}}} (\hat{W}_{i,j}^{(k)} - \bar{w}_{i,j})^2. \end{aligned}$$

The joint-level weighted temporal variance is

$$\text{Cons}_j = \frac{\sum_{i=1}^N \text{var}_{i,j} \bar{w}_{i,j}}{\sum_{i=1}^N \bar{w}_{i,j} + \varepsilon}, \quad (38)$$

where $\varepsilon > 0$ is a small numerical constant. This quantity aggregates per-point temporal variance, weighted by the average influence of joint j , so that fluctuations on heavily-used points dominate the score. Lower Cons_j indicates higher temporal stability for joint j .

Given original and fine-tuned models with corresponding scores $\text{Cons}_j^{\text{orig}}$ and $\text{Cons}_j^{\text{ft}}$, we define the per-joint improvement

$$\Delta_j = \text{Cons}_j^{\text{orig}} - \text{Cons}_j^{\text{ft}}. \quad (39)$$

Positive Δ_j means that fine-tuning reduces temporal jitter for joint j . In the main paper we use Δ_j as a diagnostic tool to report and visualize the most improved joints.

14. Additional Skinning Generation Baseline Analysis: UniRig

To further contextualize the temporal consistency problem, we also evaluated the *UniRig* skinning model [114] using the same protocol described in Sec. 13. We compare its performance against the *Puppeteer* baseline and our *SPRig* (which fine-tunes *Puppeteer*). The results are presented in Tab. 7.

Table 7. Extended Temporal Consistency Comparison for Skinning. We compare our *SPRig* against the *Puppeteer* baseline and the *UniRig* baseline. Note *UniRig*'s catastrophic failure in *SymKL*, indicating severe distributional flicker.

Method	$L_1(B, C \rightarrow A) \downarrow$	$SymKL(B, C \leftrightarrow A) \downarrow$	Entropy(diag.)
Puppeteer	1328.80	2226.63	1368.45
UniRig	1310.31	8282.43	870.32
SPRig	925.77	1084.71	1396.95

14.1. Analysis of Results

The *UniRig* skinning results strongly reinforce the central premise of our paper: state-of-the-art static models exhibit severe temporal instability when applied frame-by-frame.

L1 vs. SymKL Failure. *UniRig*'s L_1 error (1310.31) is comparable to the *Puppeteer* baseline (1328.80), suggesting a similar level of average per-point error. However, its $SymKL(B, C \leftrightarrow A)$ score is catastrophic, at 8282.43. This is nearly 4 \times worse than *Puppeteer* (2226.63) and 7.6 \times worse than our *SPRig* (1084.71).

The *SymKL* metric is highly sensitive to the shape of the predicted weight distributions. This catastrophic score indicates that *UniRig*'s predictions are not just slightly inaccurate, but are exhibiting wildly different distributional shapes between frames—a clear sign of severe temporal flicker.

The Flickering Paradox. A further insight is revealed by the Entropy metric. *UniRig* achieves the lowest entropy (870.32), indicating that its predictions are, on average, extremely sharp and confident.

This combination of very low Entropy (high confidence) and very high *SymKL* (high instability) points to a particularly severe failure mode: *UniRig* is not just uncertain about its predictions. Rather, it is flickering: it confidently assigns a point to Joint A on one frame, and then just as confidently assigns it to Joint B on the next. This behavior is the definition of temporal incoherence and is qualitatively validated in our visual examples (Fig. 6).

Conclusion. This analysis confirms that the temporal instability problem is not unique to *Puppeteer* but is a general weakness of SOTA static models, with *UniRig* exhibiting an even more severe failure mode for skinning. This data further underscores the necessity and efficacy of our *SPRig* framework, which successfully fine-tunes the *Puppeteer* baseline to achieve state-of-the-art temporal stability, dramatically outperforming both static models.